Vol. 4 No. 2 Tahun 2021

P-ISSN : 2621-0215
E-ISSN : 2621-489X

Al-Fiziya

Journal of Materials Science, Geophysics, Instrumentation and Theoretical Physics

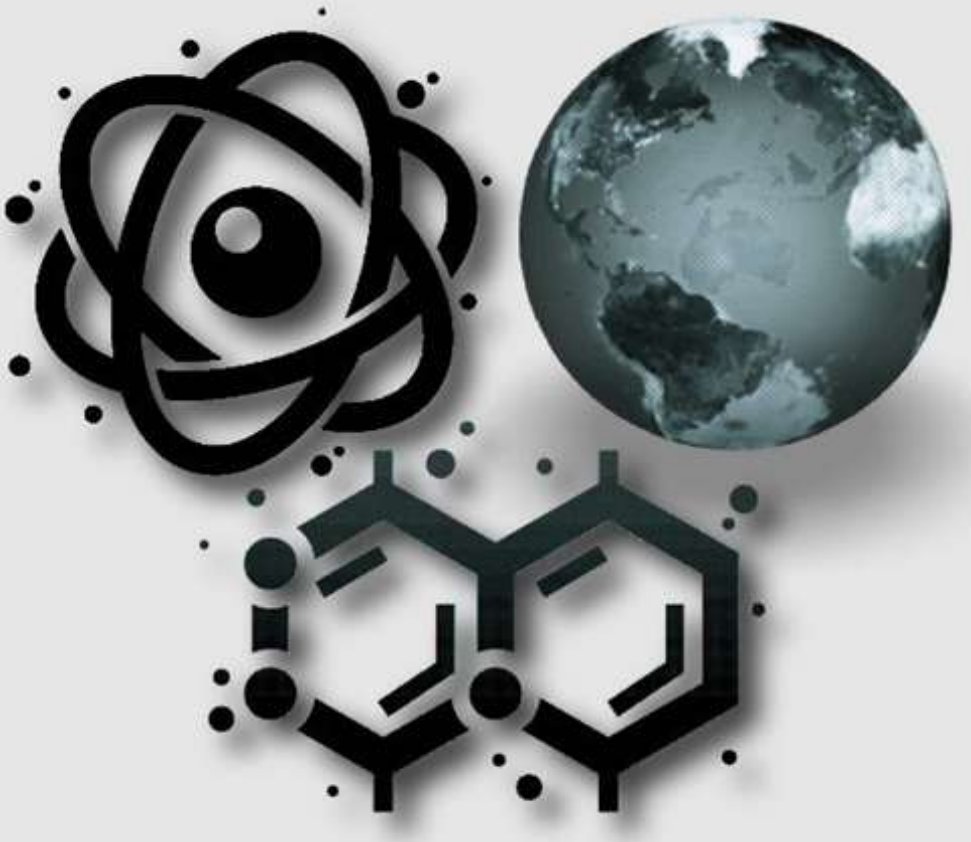

Published by
Program Studi Fisika
Fakultas Sains dan Teknologi
Universitas Islam Negeri Syarif Hidayatullah Jakarta

AL-FIZIYA:

Journal of Materials Science, Geophysics, Instrumentation, and Theoretical Physics

Vol. 4 No. 2 Tahun 2021

Alamat Redaksi
Gedung Fakultas Sains dan Teknologi Lt. 3
Jl. Ir. H Juanda No.95 Ciputat 15412 Tangerang
Telp. (6221)743731, (6221)7493315
Email: al-fiziya@uinjkt.ac.id

Published by
Program Studi Fisika, Fakultas Sains dan Teknologi
Universitas Islam Negeri Syarif Hidayatullah Jakarta

PENGANTAR REDAKSI

Assalamu'alaikum, Wr. Wb.

Puji Syukur kita panjatkan kehadirat Allah SWT, dengan terbitnya Al-Fiziya: *Journal of Materials Science, Geophysics, Instrumentation, and Theoretical Physics* Vol. 4 No. 2 Tahun 2021 dengan nomor ISSN: 2621-0215 dan E-ISSN: 2621-489X sebagai jurnal penelitian dan pengembangan ilmu fisika yang diterbitkan oleh Program Studi Fisika Fakultas Sains dan Teknologi UIN Syarif Hidayatullah Jakarta. Jurnal ini menyajikan artikel-artikel penelitian dan pengembangan terkini baik dalam Bahasa Indonesia maupun Bahasa Inggris di bidang fisika murni dan terapan, antara lain bidang fisika material, geofisika, fisika instrumentasi, dan fisika teori. Jurnal ini merupakan sarana publikasi bagi dosen dan para peneliti yang bergerak di bidang penelitian dan pengembangan ilmu fisika. Dengan demikian, melalui penerbitan jurnal ini kami memberikan kesempatan seluas-luasnya bagi siapapun yang ingin berpartisipasi dalam menyampaikan buah pikirannya melalui tulisan atau artikel yang akan kami muat pada edisi berikutnya.

Artikel yang masuk akan melalui proses seleksi oleh dewan editor dan review yang melibatkan mitra bestari baik dari para dosen ahli dibidangnya berdasarkan kesesuaian isi dan bobot karya ilmiah. Untuk informasi lengkap submit dan tata cara penulisan dalam Al-Fiziya: *Journal of Material Science, Geophysics, Instrumentation, and Theoretical Physics* dapat dilihat pada pedoman penulisan artikel di halaman akhir penerbitan atau dapat mengakses website kami di http://journal.uinjkt.ac.id/index.php/al-fiziya. Atas nama dewan redaksi, kami mengucapkan terimakasih atas dukungan dan partisipasi dari semua pihak hingga terbitnya Al-Fiziya: *Journal of Materials Science, Geophysics, Instrumentation, and Theoretical Physics.*

Editorial in chief
Sitti Ahmiatri Saptari

Daftar Isi

Vol. 4 No. 2 Tahun 2021

Available online at:
Al-Fiziya: Journal of Materials Science, Geophysics, Instrumentation and Theoretical Physics
Website: http://journal.uinjkt.ac.id/index.php/al-fiziya
Vol.4 No. 2 Tahun 2021, 74 -82

Law of Approach to Saturation for Determining Magnetic Intrinsic Behavior of $BaFe_{12-x}Mn_{x/2}Ti_{x/2}O_{19}$ and $SrFe_{12-x}Mn_{x/2}Ti_{x/2}O_{19}$

Rafael F. Maniur [1], Adam Badra Cahaya [1,†], Azwar Manaf [1]
[1]Department of Physics, Faculty of Mathematics and Natural Sciences, Universitas Indonesia Depok 16424, Indonesia

[†]adam@sci.ui.ac.id

Submitted : August 2021; Revised : December 2021; Approved : December 2021; Available Online : December 2021

Abstrak. Magnet permanen medan anisotropik yang sangat tinggi adalah sulitnya untuk menentukan sifat magnetik intrinsik jika diukur menggunakan magnetometer yang memiliki medan magnet terbatas. Model matematika Law of Approach to Saturation (LAS) menyediakan cara untuk mengukur magnet permanen, dengan medan anisotropik tinggi dengan mengoreksi data magnetisasi kurva kuadran pertama atau kurva perawan dari loop histeresis minor. Dalam penelitian ini, program komputasi LAS dilakukan untuk menghitung sifat magnetik intrinsik bahan magnetik, seperti magnetisasi saturasi, medan anisotropi dan konstanta anisotropi magnetokristalin. Data magnetisasi diperoleh dari pengukuran permagraf barium heksaferit ($BaFe_{12}O_{19}$), strontium heksaferit ($SrFe_{12}O_{19}$) dan penyerap gelombang mikro $BaFe_{12-x}Mn_{x/2}Ti_{x/2}O_{19}$ dan $SrFe_{12-x}Mn_{x/2}Ti_{x/2}O_{19}$. Pengaruh substitusi bahan barium heksaferit dan strontium heksaferit terhadap nilai magnetisasi saturasi, konstanta anisotropi dan medan anisotropik dapat dinilai dengan mengamati konfergensi nilai magnetisasi.

***Kata Kunci**: barium heksaferit; kurva hysteresis; Law of Approach to Saturation; sifat magnetic intrinsik; strontium heksaferit*

Abstract Permanent magnetic materials of very high anisotropic fields is that it is still difficult to determine the intrinsic magnetic properties, when measured using a magnetometer which has a limited magnetic field. The Law of Approach to Saturation (LAS) mathematical model provides a way to measure permanent magnets, with high anisotropic fields by correcting the magnetization data of the first quadrant curve or the virgin curve of the minor hysteresis loop. In this research, a computational LAS program was conducted to compute the intrinsic magnetic properties of magnetic materials, such as saturation magnetization, anisotropy field and magnetocrystalline anisotropy constant. Magnetization data of barium hexaferrite ($BaFe_{12}O_{19}$), strontium hexaferrite ($SrFe_{12}O_{19}$), $BaFe_{12-x}Mn_{x/2}Ti_{x/2}O_{19}$ and $SrFe_{12-x}Mn_{x/2}T_{ix/2}O_{19}$ are analyzed. The convergences of magnetization were assessed to determine the effect of substitution on barium hexaferrite and strontium hexaferrite materials on saturation magnetization values, anisotropy constants and anisotropic fields. We determine the appropriate lower limit for LAS method to give correct values of saturation magnetization values, anisotropy constants and anisotropic fields.

***Keywords**: barium hexaferrite; hysteresis loop; intrinsic magnetic properties; Law of Approach to Saturation; strontium hexaferrite.*

DOI : *10.15408/fiziya.v4i2.22206*

P-ISSN: 2621-0215, E-ISSN: 2621-489X

INTRODUCTION

To achieve a high energy density, a permanent magnet must have high remanence and coercivity values. The magnetic phase must have a high anisotropic field value so that the coercivity value is high. Both remanent and coercivity are derived from the main hysteresis loop or major hysteresis loop. Thus, to magnetize permanent magnets that have high coercivity, a high external magnetic field is required. As an illustration, the magnetic anisotropic field of Nd-Fe-B is 5.4 MA/m or 67.5 kOe [1], [2]. Therefore, a magnetizing field of 67.5 kOe is required to obtain the main hysteresis loop. This can only be achieved when using magnet magnets from superconductors[3]. However, at this time magnetization generally uses an electromagnet which can only produce a magnetic field external magnet of 12 kOe to 15 kOe [4]. Therefore, another method is needed to obtain the main hysteresis loop from the use of such a low external magnetic field.

The anisotropic field itself depends on the distance and direction of the lattice of a material to the magnetic field [5]–[7] and affects the shape of the hysteresis loop of a material. The high anisotropic field in some types of materials causes the need for new equipment to study these materials, while the magnetometer equipment can only measure in fields around 1.2 T to 1.5 T [8]. When used, the material in the magnet will produce a hysteresis loop. minor, which unfortunately does not describe the true state of the magnetic material under study. The minor loop is not a true loop, while to obtain magnetic properties, a major hysteresis loop is needed, which is difficult to obtain when measured only with a weak field magnetometer.

The use of the LAS (Law Approach of Saturation) method [9]–[11] is intended to overcome the difficulties of studying materials with very high anisotropic fields. In this method, it is hoped that materials with minor loops can be converted into major hysteresis loops, so that their magnetic properties can be explained. In addition, the LAS method can determine the intrinsic properties of a material, namely anisotropic fields, anisotropic constants, and saturation [10], which are useful for the purposes of making magnetic materials or for modifying these magnetic materials.

LAW OF APPROACH TO SATURATION METHOD

For this study, we were looking for material data sets of Mn-Ti-substituted barium hexaferrite ($BaFe_{12-x}Mn_{x/2}Ti_{x/2}O_{19}$) and strontium hexaferrite ($SrFe_{12-x}Mn_{x/2}Ti_{x/2}O_{19}$). Material data sets were using Permagraph from Ref. [4]. These material data sets were used to validate the executed program as well as for hysteresis loop correction purposes, with the magnetization data taken is the minor hysteresis loop of magnetization data in the first quadrant *i.e.* from the beginning of the magnetization until the magnetization value reaches the peak. Figure 1 shows the hysteresis loop and the virgin curve of the selected data of Barium Hexaferrite and Strontium Hexaferrite, to be used for validation.

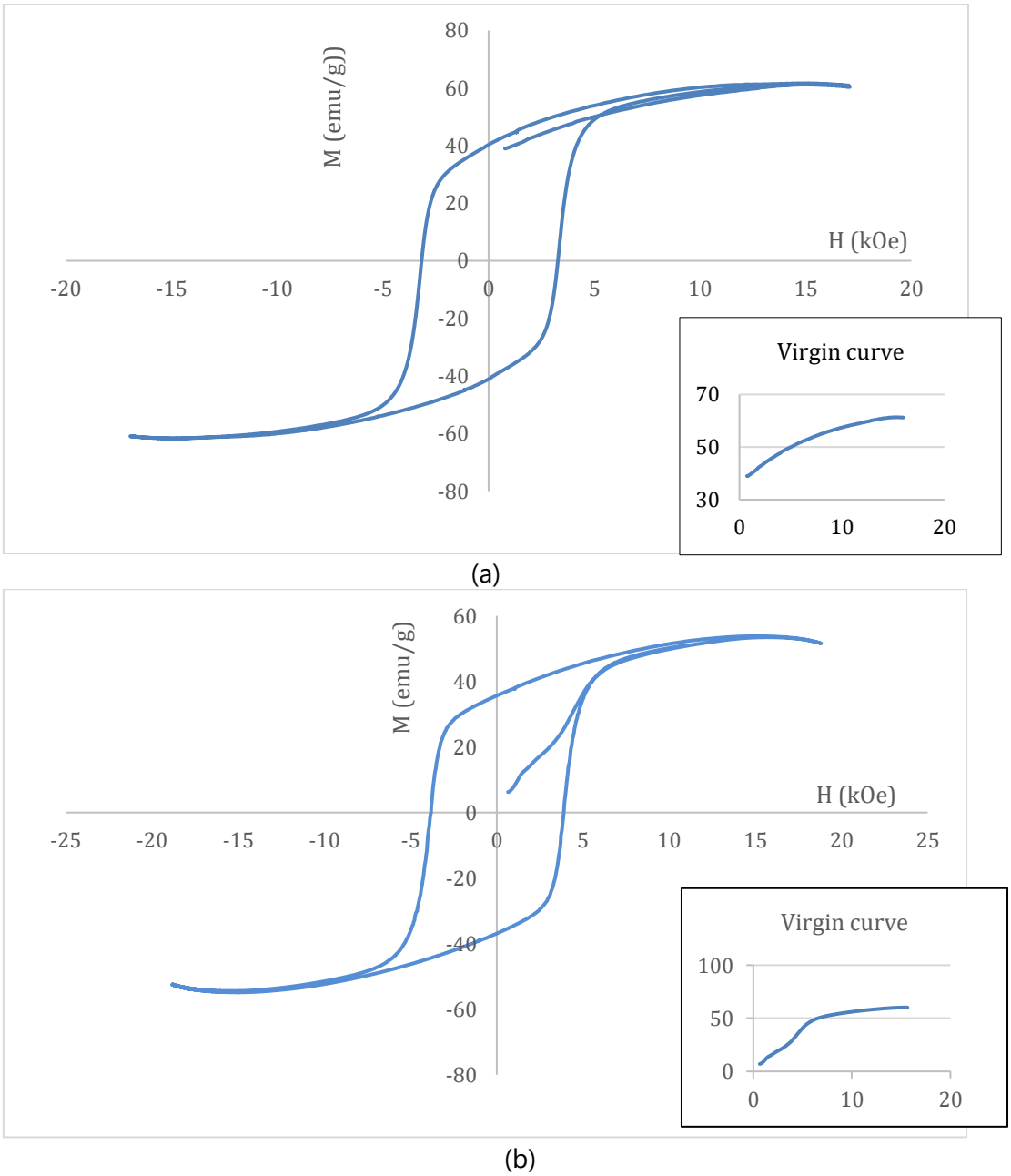

Figure 1. Hysteresis Loop and virgin curve (inset) of (a) barium hexaferrite ($BaFe_{12}O_{19}$) and (b) strontium hexaferrite ($SrFe_{12}O_{19}$)

As can be seen from Figure 1 saturation in magnetization occurs when the magnetization of a material stops or rises very slowly when a very large external magnetic field is applied. This behaviour of magnetization curve is often called Law of Approach to Saturation (LAS)[12]. While there are variations in the approximation for LAS, in this study we compare 4 models: Akulov [10] , Brown [11] , Grössinger [12] and Néel [13] . The most general the most general of them is Grössinger equation.

$$M = Ms\left[1 - \frac{a}{H} - \frac{b}{H^2} - \frac{c}{H^3}\right] + \chi H \qquad (1)$$

This equation is a generalized equation from Akulov approximation ($a = c = \chi = 0$) [10] , Néel approximation ($c = \chi = 0$) [13] and Brown approximation ($c = 0$) [11] . Here M_s is magnetization saturation, χ is magnetic susceptibility, $a > 0$ is inhomogeneity parameter,

b and c are related to magnetic anisotropy [12] . While in Ref. [12] another $\sqrt{H}$ term that arises from spin wave is considered, we ignore this term for better comparison with other LAS models. The value of b is related to anisotropy constant K_1 (or anisotropy field $H_a = 2K_1/M_s$) as follows [6], [12] .

$$b = \frac{8}{105} \times \frac{K_1^2}{M_s^2} = \frac{2}{105} H_a^2 \quad (2)$$

Eq. (2) shows that with a positive b value, the intrinsic magnetic properties of a material, such as anisotropy constant and anisotropic field can be determined. A positive value for the constant b also indicates that the field is sufficient to produce the calculated Ms value of a material, while a negative value indicates that the applied magnetic field is not sufficient to make a material achieve saturation magnetization.

RESULTS AND DISCUSSION

To determine a suitable model to find the saturation magnetization value in a material, we fit the data in Figure 1(a) with LAS models in Eq. (2). As shown in Figure 2, the application of the Brown model and the Grössinger model produces a magnetization value that continues to increase when an external magnetic field H is up to 40 kOe. These models are not in line with the principle of saturation of the magnetization. Néel and Akulov models, however, shows signs of reaching the saturation magnetization value at a certain external field value. The plot of the magnetization value calculated by the two models shows a difference in the value. The results obtained that the saturation magnetization values in the Néel and Akulov models are 62 emu/gr and 58 emu/gr, respectively.

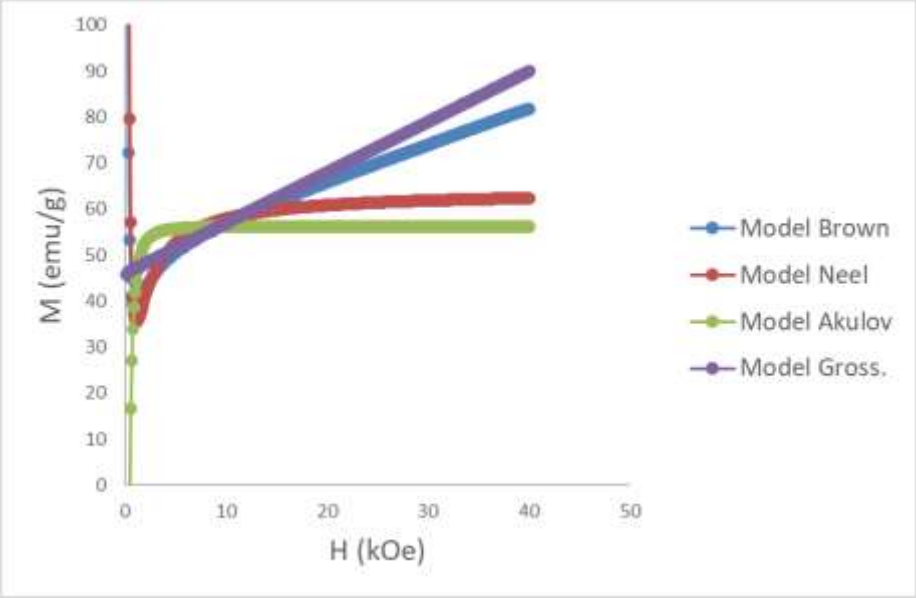

Figure 2. M vs H of Law of Approach to Saturation (LAS) models of materials $BaFe_{12}O_{19}$.

The M_s value of the computational result is compared with the Ms value of barium hexaferrite material from the literature, which is M_s = 72 emu/g or 0.48 T [14] . We can conclude that M_s value in the Néel model is closer to the literature value compared to

the saturation magnetization value in the Akulov models. Therefore, we will use Néel model for further fitting.

$$M = M_s\left[1 - \frac{a}{H} - \frac{b}{H^2}\right] \quad (3)$$

To ensure M_s convergence, we determined a suitable lower limit to determine the value of M_s. We suggest that a good lower limit for fittings occurs by plotting the magnetization saturation value when fitting at some variation of the lower limit value against a given external field, with error bars presented to help seeing the convergence of the magnetization values on a visible graph.

Lower Limit Fitting for Realistic a and b

A good lower limit is determined when the M_s error value generated when fitting with a lower limit variation is small, and there is convergence (no change) in the M_s value after setting the lower limit variation. These conditions are then applied to determine the saturation magnetization value and a good field lower limit value for this material. A plot of M_s vs lower limit H with variation of 1 kOe to 10 kOe of $BaFe_{12}O_{19}$ composition is shown on figure 3. When the H field around 8500 Oe the M_s value begins to decrease from the Ms value of about 68 emu/g, which is close to the reference value M_s of $BaFe_{12}O_{19}$ (72 emu/gr). This saturation magnetization value also improves the saturation magnetization value obtained before the lower limit is applied. This shows that a good lower limit will produce a good saturation magnetization value as well.

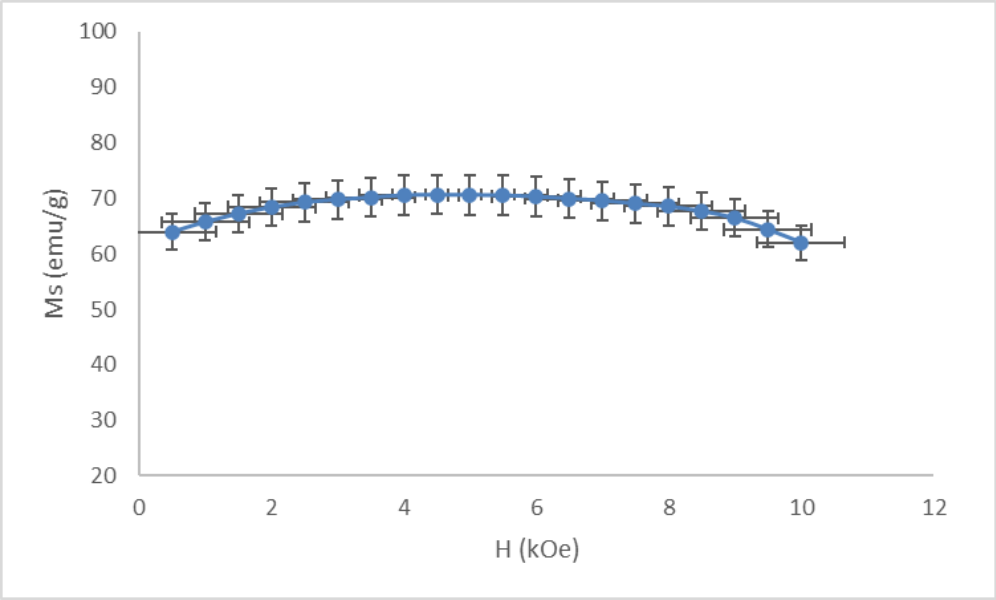

Figure 3. LAS method requires appropriate choice for its lower limit H. Here the fittingresult for Ms is plotted against the lower limit H that is varied between 1 kOe to 10 kOe on the composition of $BaFe_{12}O_{19}$.

Next, a and b are observed to determine the right lower limit as it is very influential on the calculation results of the intrinsic magnetic properties of a material. The value of a and b are illustrated in Figure 5. Since $a > 0$ and $b = 2H_a^2/105$, the determination of

the lower limit value requires that the values of a and b are positive quantities. Figure 4 indicates that a and b are positive for 8.5 to 9.5 kOe.

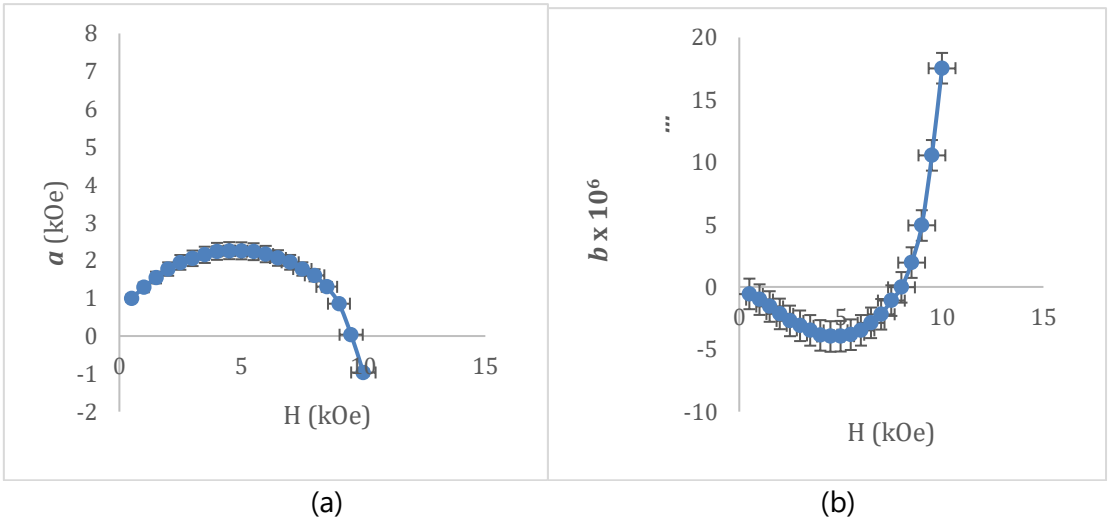

(a) (b)

Figure 4. Compared to Ms, values of (a) *a* constant and (b) *b* constant are plot against the lower limit H for LAS method of $BaFe_{12}O_{19}$ material.

Table 1 summarized the calculation results of the LAS method for pure BHF samples. We calculated the intrinsic magnetic properties of pure BHF materials and compared them with reference values. The calculated data is also used to determine a suitable lower bound. These intrinsic magnetic properties include the value of saturation magnetization, the value of the anisotropy constant (K_1) and the anisotropy field (H_a). The lower limit between 8.5 kOe to 9.5 kOe was then chosen to find the value of the anisotropy constant K1 and the anisotropic field Ha at each lower limit.

Table 1. The intrinsic magnetic properties resulting from the variation of the lower limit between 8.5 kOe, 9 kOe, and 9.5 kOe in $BaFe_{12}O_{19}$ materials compared with literature values [14]

Lower Limit	M_s(emu/g)		K_1 (10^6 erg/cc)		H_a (kOe)	
(kOe)	Fit.	Lit.	Fit.	Lit.	Fit.	Lit.
8.500	68	72	3.42	3.3	10.123	16.994
9.000	66	72	5.34	3.3	16.079	16.994
9.500	64	72	7.57	3.3	23.535	16.994

By choosing 8.5 kOe as lower limit for LAS analysis, the anisotropic constant and the anisotropic field yield values of 3.42 x 106 erg/cc and 10.123 kOe, respectively, approaching the theoretical value of 3.3 x 10^6 erg/cc and 16,994 kOe [17]. In Figure (43), the lower limit values of the 2.0 kOe and 8.5 kOe external fields produce the same saturation magnetization value, but because the lower limit of 2.0 kOe produces a negative *b* constant value, this situation can be ignored. This shows that the lower limit of the external magnetic field of 8.50 kOe is a good lower limit for determining the intrinsic magnetic properties of pure $BaFe_{12}O_{19}$ materials.

Saturation Magnetization and Anisotropy field of $BaFe_{12-x}Mn_{x/2}Ti_{x/2}O_{19}$, and $SrFe_{12-x}Mn_{x/2}Ti_{x/2}O_{19}$

After validating the calculated data from the LAS method of $BaFe_{12}O_{19}$ magnetization data, this computational program can be applied to calculate the intrinsic parameters of the synthesized material. In this section, the results of the calculation of the LAS method on data from two different Radar Absorbing Material (RAM) samples are discussed, namely $BaFe_{12-x}Mn_{x/2}Ti_{x/2}O_{19}$, and $SrFe_{12-x}Mn_{x/2}Ti_{x/2}O_{19}$, which were calculated using the Néel model with limits under an external field of 500 kA/m respectively. with x = 0.1 sample of both RAM is given. We note here that values of a for $SrFe_{12-x}Mn_{x/2}Ti_{x/2}O_{19}$ are small enough, such that Néel model does not differ much from Akulov model for $SrFe_{12-x}Mn_{x/2}Ti_{x/2}O_{19}$.

Table 2 and 3 are the summary of intrinsic magnetic values of both RAM materials of $BaFe_{12-x}Mn_{x/2}Ti_{x/2}O_{19}$, and $SrFe_{12-x}Mn_{x/2}Ti_{x/2}O_{19}$, respectively The substitution of Mn2+ and Ti4+ ions to Fe3+ ions change the intrinsic magnitude of the material phase[18] . There is a downward trend in the values of M_s, H_a, K_1, and b when Mn-Ti substitution is given (x > 0). It may be because the substitution of Mn-Ti ions in both RAM material influences the dimensions of the $BaFe_{12}O_{19}$ crystal unit cell due to the difference in the size of the radii of Mn and Ti ions with Fe ions [17].

The virgin curve magnetization data were obtained with a very limited external magnetic field of 12 – 15 kOe or 960 - 1200 kA/m. The fitting result have been summarized for the respective RAM samples in Tables 2 and 3. The intrinsic value of the magnetic properties of the magnetic phase of the material is expected to be used by other researchers to conduct data analysis and further discussion of the experimental test results.

Table 2. Output of computational results of the LAS sample $BaFe_{12-x}Mn_{x/2}Ti_{x/2}O_{19}$ (x=0; 0.1; 0.3 and 0.5)

Comp. X	M_s (T)	H_a (kA/m)	$K_1 \times 10^5$ (J/m^3)	B $(kA/m)^2$
0	0,418	1613	3,37	49583
0,1	0,433	1698	3,67	54932
0,3	0,411	1444	2,97	39767
0,5	0,391	1268	2,48	30631

Table 3. Output of computational results of the LAS sample $SrFe_{12-x}Mn_{x/2}Ti_{x/2}O_{19}$ (x=0; 0.1; 0.3; 0.5; and 1.0)

Comp. X	M_s (T)	H_a (kA/m)	$K_1 \times 10^5$ (J/m^3)	b $(kA/m)^2$
0	0,36	1739	3,13	57460
0,1	0,321	1659	2,66	52485
0,3	0,338	1445	2,44	39776
0,5	0,344	1577	2,71	47375
1,0	0,36	1498	2,7	42769

CONCLUSION

From this study, we can conclude that the Law of Approach to Saturation (LAS) method using magnetization data from the minor loop works based on an appropriate mathematical model. The Néel model dcan be applied for both namely $BaFe_{12-x}Mn_{x/2}Ti_{x/2}O_{19}$, and $SrFe_{12-x}Mn_{x/2}Ti_{x/2}O_{19}$. Lower limit selection for this study plays a significant part since it greatly determines the convergence of saturation magnetization. Furthermore, lower limit selection is required to determine correct values for a and b. Positive values of a and b can be obtained by selecting 8.5 kOe lower limit for LAS method.

ACKNOWLEDGMENTS

The authors would thank L. Darmawan for experimental discussion.

REFERENCES

[1] J. J. Croat, J. F. Herbst, R. W. Lee, and F. E. Pinkerton, "High-energy product Nd-Fe-B permanent magnets," *Applied Physics Letters*, vol. 44, no. 1, pp. 148–149, Jan. 1984, doi: 10.1063/1.94584.

[2] J. Mohapatra and J. P. Liu, "Chapter 1 - Rare-Earth-Free Permanent Magnets: The Past and Future," vol. 27, E. B. T.-H. of M. M. Brück, Ed. Elsevier, 2018, pp. 1–57. doi: https://doi.org/10.1016/bs.hmm.2018.08.001.

[3] J. van Nugteren, "High Temperature Superconductor Accelerator Magnets," 2016.

[4] L. Darmawan, Suparno, and A. Manaf, "Enhancement of Magnetic and Microwave Absorbing Properties of [Ba (Fe, Mn, Ti)12 O19]1-x–[CoFe12 O4] x (x = 0.2; 0.5; 0.8) Composites," *Journal of Physics: Conference Series*, vol. 1485, p. 12046, 2020, doi: 10.1088/1742-6596/1485/1/012046.

[5] A. Renuka Balakrishna and R. D. James, "A tool to predict coercivity in magnetic materials," *Acta Materialia*, vol. 208, p. 116697, 2021, doi: https://doi.org/10.1016/j.actamat.2021.116697.

[6] F. Kools and A. Morel, "Ferrite Magnets: Improved Performance," K. H. J. Buschow, R. W. Cahn, M. C. Flemings, B. Ilschner, E. J. Kramer, S. Mahajan, and P. B. T.-E. of M. S. and T. Veyssière, Eds. Oxford: Elsevier, 2004, pp. 1–5. doi: https://doi.org/10.1016/B0-08-043152-6/01908-2.

[7] P. Gruszecki, C. Banerjee, M. Mruczkiewicz, O. Hellwig, A. Barman, and M. Krawczyk, "Chapter Two - The influence of the internal domain wall structure on spin wave band structure in periodic magnetic stripe domain patterns," in *Recent Advances in Topological Ferroics and their Dynamics*, vol. 70, R. L. Stamps and H. B. T.-S. S. P. Schultheiß, Eds. Academic Press, 2019, pp. 79–132. doi: https://doi.org/10.1016/bs.ssp.2019.09.003.

[8] R. Prigl, U. Haeberlen, K. Jungmann, G. zu Putlitz, and P. von Walter, "A high precision magnetometer based on pulsed NMR," *Nuclear Instruments and Methods in Physics Research Section A: Accelerators, Spectrometers, Detectors and Associated Equipment*, vol. 374, no. 1, pp. 118–126, 1996, doi: https://doi.org/10.1016/0168-9002(96)37493-7.

[9] E. C. Devi and I. Soibam, "Effect of Zn doping on the structural, electrical and magnetic properties of MnFe2O4 nanoparticles," *Indian Journal of Physics*, vol. 91, no. 8, pp. 861–867, 2017, doi: 10.1007/s12648-017-0981-7.

[10] H. Zhang, D. Zeng, and Z. Liu, "The law of approach to saturation in ferromagnets originating from the magnetocrystalline anisotropy," *Journal of Magnetism and Magnetic*

Materials, vol. 322, no. 16, pp. 2375–2380, 2010, doi: https://doi.org/10.1016/j.jmmm.2010.02.040.

[11] B. D. Cullity and C. D. Graham, *Introduction to Magnetic Materials*. John Wiley & Sons, 2011.

[12] R. Grössinger, "A critical examination of the law of approach to saturation. I. Fit procedure," *physica status solidi (a)*, vol. 66, no. 2, pp. 665–674, Aug. 1981, doi: https://doi.org/10.1002/pssa.2210660231.

[13] N. S. Akulov, "Über den Verlauf der Magnetisierungskurve in starken Feldern," *Zeitschrift für Physik*, vol. 69, no. 11, pp. 822–831, 1931, doi: 10.1007/BF01339465.

[14] W. F. Brown, "Theory of the Approach to Magnetic Saturation," *Physical Review*, vol. 58, no. 8, pp. 736–743, Oct. 1940, doi: 10.1103/PhysRev.58.736.

[15] R. Grössinger, "A critical examination of the law of approach to saturation. I. Fit procedure," *physica status solidi (a)*, vol. 66, no. 2, pp. 665–674, Aug. 1981, doi: https://doi.org/10.1002/pssa.2210660231.

[16] L. Néel, "Relation entre la constante d{\textquotesingle}anisotropie et la loi d{\textquotesingle}approche à la saturation des ferromagnétiques," *Journal de Physique et le Radium*, vol. 9, no. 6, pp. 193–199, 1948, doi: 10.1051/jphysrad:0194800906019300.

[17] R. C. Pullar, "Hexagonal ferrites: A review of the synthesis, properties and applications of hexaferrite ceramics," *Progress in Materials Science*, vol. 57, no. 7, pp. 1191–1334, 2012, doi: https://doi.org/10.1016/j.pmatsci.2012.04.001.

[18] G. Turilli, F. Licci, S. Rinaldi, and A. Deriu, "Mn2+, Ti4+ substituted barium ferrite," *Journal of Magnetism and Magnetic Materials*, vol. 59, no. 1, pp. 127–131, 1986, doi: https://doi.org/10.1016/0304-8853(86)90019-3.

[19] M. H. Shams, A. S. H. Rozatian, M. H. Yousefi, J. Valíček, and V. Šepelák, "Effect of Mg2+ and Ti4+ dopants on the structural, magnetic and high-frequency ferromagnetic properties of barium hexaferrite," *Journal of Magnetism and Magnetic Materials*, vol. 399, pp. 10–18, Feb. 2016, doi: 10.1016/J.JMMM.2015.08.099.

Available online at:
Al-Fiziya: Journal of Materials Science, Geophysics, Instrumentation and Theoretical Physics
Website: http://journal.uinjkt.ac.id/index.php/al-fiziya
Vol. 4 No. 2 Tahun 2021, 83 - 88

Mapping of Peak Ground Acceleration (PGA) using The Kawashumi Model for Sumatera

Tati Zera[1,†]

[1]Department of Physics, Faculty of Science and Technology, Syarif Hidayatullah Islamic State University, Ir. H. Djuanda St, No.95, Cempaka Putih, Ciputat, South Tangerang, Banten 15412, Indonesia
[†]tati_zera@uinjkt.ac.id

Submitted : November 2021; Revised : December 2021; Approved : December 2021; Available Online : December 2021

Abstrak. Posisi pantai barat pulau Sumatera yang merupakan wilayah pertemuan lempeng Eurasia dan IndoAustralia memiliki seismisitas yang tinggi karena aktivitas tektoniknya. Tingkat seismisitas yang tinggi ini mengindikasikan sangat banyaknya kejadian gempabumi yang memberikan efek gerakan tanah. Penelitian ini melakukan perhitungan dan analisis terhadap percepatan gerakan tanah maksimum *(Peak Ground Acceleration - PGA)* sebagai efek kejadian gempabumi merusak di Sumatera selama 100 tahun sejak 1 Januari 1920 - 31 Desember 2020 berdasarkan model Kawashumi. Hasil perhitungan memberikan nilai PGA dalam rentang 388.190 – 4008.210 gal dengan nilai maksimum 4199,45 gal pada 3.295°LU, 95.982°BT yang disebabkan gempa 9,1 M di Pulau Andaman pada 24 Desember 2004. Sementara nilai PGA minimum sebesar 314,9 gal yang terletak di 4.438°LS - 101.367°BT yang disebabkan gempa Bengkulu 8,4 M. Pemetaan hasil perhitungan ini menghasilkan pola PGA yang tinggi di utara Sumatera dan dan semakin berkurang ke arah selatan. Hal ini memperlihatkan bahwa gempabumi - gempabumi merusak yang terjadi di utara pulau Sumatera lebih memberikan resiko yang besar terhadap pergerakan tanah dibandingkan gempabumi-gempabumi merusak yang terjadi di selatan pulau Sumatera. Pola PGA ini berbeda dengan beberapa penelitian sebelumnya.
Kata Kunci *: Peak Ground Acceleration, Kawashumi, seismisitas.*

Abstract. The position of the west coast of the island of Sumatra, which is the meeting point of the Eurasian and Indo-Australian plates, has high seismicity due to its tectonic activity. This high level of seismicity indicates that many earthquakes have an effect on ground motion. This study calculates and analyses the maximum ground motion acceleration (Peak Ground Acceleration - PGA) as the effect of destructive earthquakes in Sumatra for 100 years from January 1, 1920 - December 31, 2020, using the Kawashumi model. The calculation results give PGA values in the range of 388,190 – 4008,210 gal with a maximum value of 4199.45 gals at 3,295°N, 95,982°E caused by the 9.1 M earthquake on Andaman Island on December 24, 2004. While the minimum PGA value is 314.9 gals located at 4.438°LS - 101.367°BT caused by the Bengkulu 8.4 M earthquake. This calculation results in a map showing a high PGA pattern in the northern part of Sumatra and decreasing towards the south. This indicates that destructive earthquakes that occur in the northern part of Sumatra Island pose a greater risk of ground movement that destructive earthquakes that occur in the southern part of Sumatra Island. This PGA pattern is different from several previous studies.
Keywords : *Peak Ground Acceleration, Kawashumi, seismicity.*

DOI : *10.15408/fiziya.v4i2.23282*

P-ISSN: 2621-0215, E-ISSN: 2621-489X

INTRODUCTION

A abrupt displacement of the earth's plates produced by tectonic or volcanic activity, as well as landslides, is known as an earthquake. Because of the meeting route of tectonic plates, the Indo-Australian Plate, the Eurasian Plate, and the Pacific Plate, earthquakes are highly prevalent in Indonesia. Sumatra is one of the islands that is regularly struck by earthquakes. This island is situated near the subduction zone formed by the junction of the Indian-Australian plate and the Eurasian plate. A Semangko fault system runs the length of the island, while a Mentawai fault system runs the length of the offshore. Ground movement caused by earthquakes causes damage to houses and other structures. A Peak Ground Acceleration (PGA) map is required as a precautionary step to mitigate the effects of the earthquake. PGA may be measured using an accelerometer as a result of an earthquake. It is, however, difficult to apply it over vast regions. Another method for determining the PGA value is to use the earthquake accumulation. These values may then be plotted, giving an overview of which locations are sensitive to ground movement and which are not. The peak ground acceleration will vary every time an earthquake happens due to the accumulation of shocks, thus this map will need to be updated at regular intervals. [1].

For each earthquake, PGA is a disruption that is measured. The maximum ground acceleration, or PGA, is chosen to be mapped in order to have a better knowledge of a location's most severe effects. The greatest peak ground acceleration is the highest figure ever recorded in a location as a result of an earthquake. The bigger the PGA value that has occurred in a location, the higher the hazard and risk of an earthquake occurring. Because ground acceleration is the most important component that impacts building design and produces a uniform moment of force at all places of the structure, it is the starting point for earthquake-resistant building calculations.

A lot of researchers have studied PGA in different ways. Ground motion and subduction zones have been empirically linked by Atkinson and Boore [2]. Campbell [3] uses the Hybrid Empirical Method in Ground Motion as well. Megawati investigated the attenuation of ground motion for the big earthquake in Sumatra [4] in PGA studies performed individually in many locations of Indonesia. For a micro-zoning analysis of Jakarta, Irsham et al. produced seismic risk maps for the islands of Sumatra and Java [5]. Tati Zera et al., compare PGA maps for the Bengkulu area using three alternative models [6]. Based on Kawashumi models, this study calculates and maps the PGA value for Sumatera as locations with strong seismic activity. The 2011 Tohoku Earthquake [7] was investigated using these Kawashumi models. This model was also utilized to compare the estimated PGA value to the accelerograph data in Cilacap after the 6.1 M earthquake on January 25, 2014 [8]. This study will put Kawashumi's model to the test by looking at the ground motion patterns created by this PGA model over a 100-year period in Sumatra.

DATA AND METHOD

There are many PGA models proposed by experts, both to calculate PGA on the surface and in bedrock. No fewer than 20 PGA formulations were submitted by Douglas in 1991 and became a reference for various research on PGA [9]. However, this research will use Kawashumi's model as used in [8] in the form

$$\log \alpha = M_s - 5{,}4 - 0{,}00084\,(R - 100) + (\log \frac{100}{R}) \times \frac{1}{0{,}43429} \quad (1)$$

where α is the PGA value in gal, Ms is the earthquake's magnitude at the surface, and R is the distance to the hypocentre (km). Because the calculated PGA is the PGA value on the surface, it is necessary to first convert the earthquake into a surface magnitude. The R-value is obtained by determining the depth of the earthquake center (hypocentre) and the distance from the epicenter to the measuring station (in this case, the corner points of the grid marked on the map).

The data used in this research is the incidence of destructive earthquakes within a period of 100 years from January 1, 1920, to December 31, 2020, in Sumatra with M>5 and a depth of hypocentre (h) < 60 km. The data plot on the base map of the island of Sumatra can be seen in Figure 1, which shows the fairly high seismicity of the island of Sumatra along its west coast. The destructive earthquakes spread quite widely and evenly in the western part, but they were decreasing and did not occur in the eastern part of the island of Sumatra. The epicentre of the earthquake is mostly in the sea, and only a small part is in the region of the mainland. These earthquakes along the coast are generally subduction earthquakes. Only a small part of it is the earthquakes from the Mentawai fault. While the earthquakes on the mainland of Sumatra are earthquakes with an active fault source from the Semangko fault segment, almost all of these destructive earthquakes are caused by three tectonic frameworks on the island of Sumatra, the subduction zone, the Mentawai fault, and the Semangko fault [10].

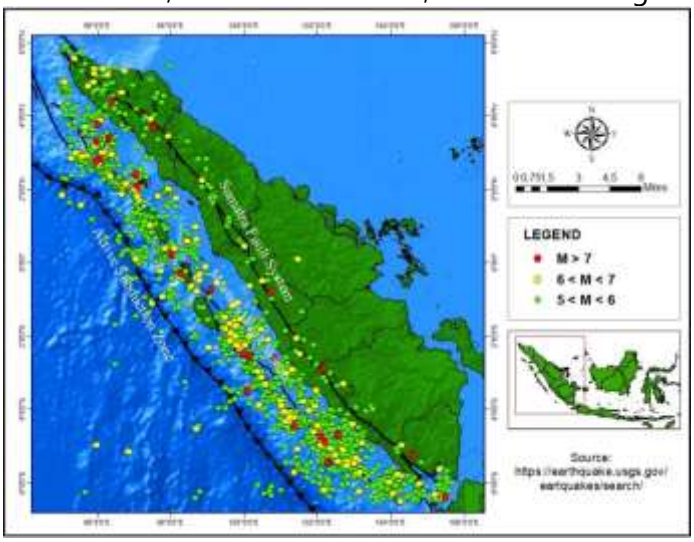

Figure 1. Sumatera Seismicity Map in 1920 - 2020

The data used in this study was obtained from the official website of the United States Geological Survey (USGS) with a total of 1757 destructive earthquakes, each consisting of 1580 earthquakes with 5<M<6, 152 earthquakes with 6<M<7, and only 25 earthquakes with M>7. The distribution of earthquakes based on 5 years of occurrence can be seen in Figure 2 below.

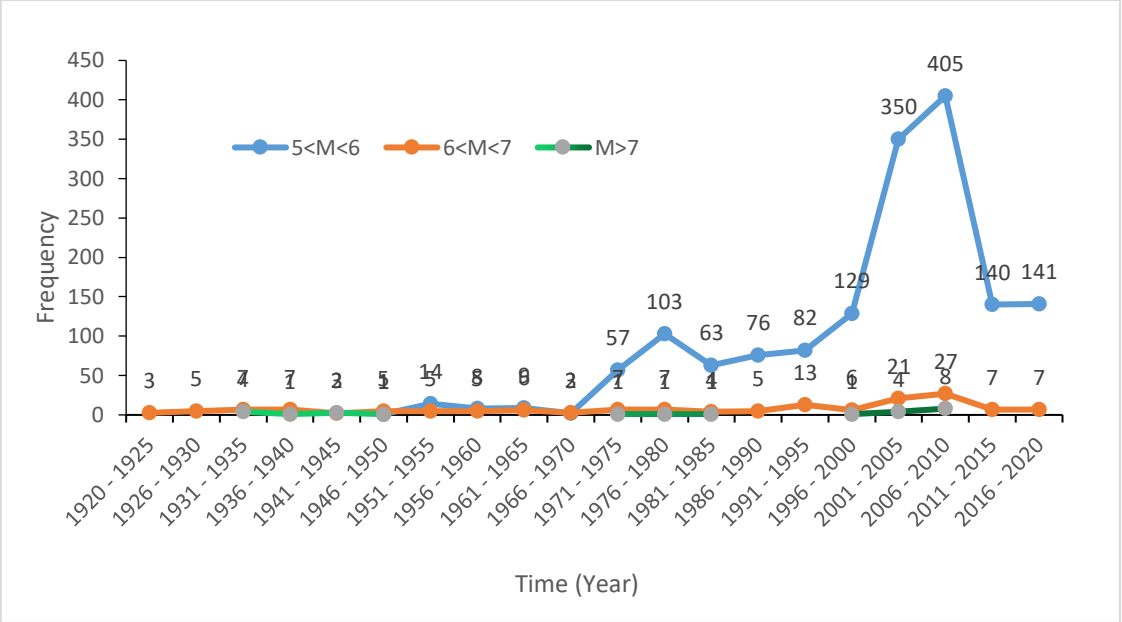

Figure 2. Sumatra Earthquakes Data 1920-2020

Earthquakes data as shown in Figure 2 shows that earthquakes with a magnitude range of 5–6 experienced an increase in the number of events during the period 1966–2010 and reached a peak of 405 at the end of this range. This condition is depicted by the blue line on the chart. Meanwhile, earthquakes with a magnitude of 6–7 showed an almost constant number of events in each period, although 2001–2010 also showed an increase. It is marked with an orange line. Large earthquakes with a magnitude > 7, on the graph marked with a green line, occurred discretely in 3 periods: 1931–1950, 1971–1985, and 1996–2010. Overall, the graph shows a significant increase in the incidence of earthquakes for all three classifications in the range of 1991–2015.

RESULT AND DISCUSSION

The PGA calculation using Kawashumi's model with 1757 data on the occurrence of destructive earthquakes in Sumatra at the geographical boundaries of 6°N - 6.5°S and 95°E - 106.5°E was carried out by making a 2o grid, which resultedin a PGA in the range of 388.190 - 4008.210 gal. This calculation results in the maximum PGA being 4199.45 gal, located at 3.295°N and 95.982°E caused by the 9.1 M earthquake in Andaman on December 24, 2004. This earthquake has also caused a large tsunami that has hit and damaged Aceh. While the minimum PGA is 314.9 gal located at 4.438°S,101.367°E which is caused by the 8.4 M Bengkulu earthquake on 12 September 2007. The results of the PGA calculation are then mapped to see the ground motion pattern. This map is shown in Figure 3 below.

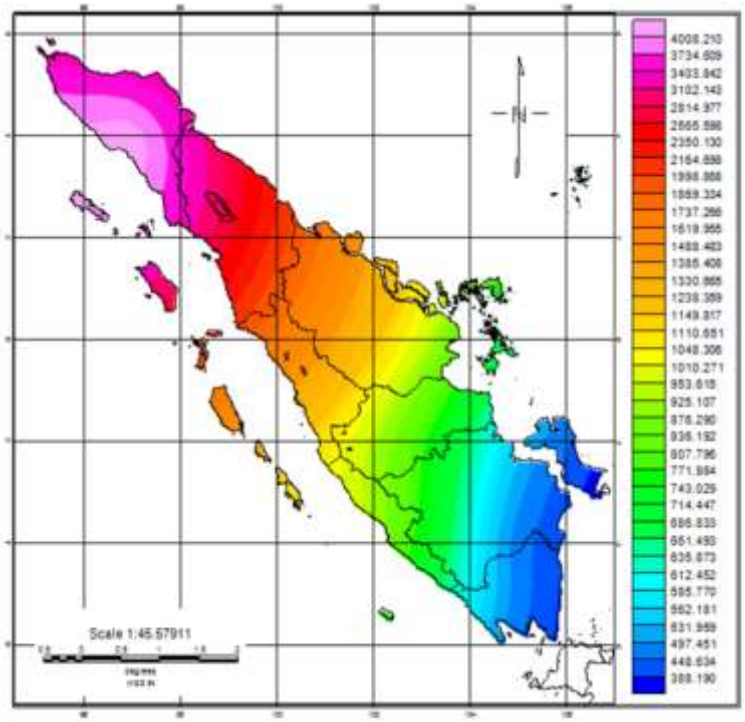

Figure 3. PGA map of Sumatera with Kawashumi's Model

The resulting map shows a high change in the PGA value in the north of Sumatra, which continues to decline towards the south. This is indicated by gradations of pink, red, and light blue and dark blue at the southern end. At first glance, this looks very different from the seismicity pattern of the island of Sumatra, as shown in Figure 1, where the seismicity density is concentrated evenly along the coast of Sumatra. However, if we look in more detail, the distribution of large earthquakes marked in red on the seismicity map tends to be more concentrated in the northern part than in other regions. This concentration of large earthquakes causes the PGA value on the northwest coast of Sumatra to be higher.

Although it does not follow the tectonic framework of the island of Sumatra, which has three active tectonic arrangements in the form of a subduction zone along the west coast, the Mentawai fault, and the Semangko fault along the mainland of Sumatra, all three are parallel to each other [10], but the PGA pattern generated using the Kawashumi model formed a different pattern due to the concentration of large earthquake events in the northern part of Sumatra. This is what causes the difference.

CONCLUSION

The determination of the peak ground acceleration (PGA) value that has been carried out using the Kawashumi model in this study, based on a catalogue of destructive earthquakes for 100 years in Sumatra, has resulted in a pattern that does not follow the tectonic setting of the island of Sumatra. The pattern formed shows a change in the high PGA value gradually decreasing from North Sumatra to the South, caused by the concentration of large earthquakes in North Sumatra. Calculation of the data with the limits used has resulted in PGA values in the range of 388.190–4008.210 gal with a maximum value of 4199.45 gal, which is located at 3.295°N and 95.982°E, caused by the 9.1 M earthquake on Andaman Island on December 24, 2004. Meanwhile, the minimum value is 314.9 gal, located at 4,438°S and 101.367°E, which was caused by the Bengkulu

8.4 M earthquake. The pattern of ground motion risk will be like this pattern if the PGA value is converted to the MMI scale. This conversion can be carried out in future research, even using other empirical models.

REFERENCES

[1] Masyhur Irsyam et.al., 2010. Tim Revisi Peta Gempa Indonesia, *Ringkasan Hasil Studi Tim Revisi Peta Gempa Indonesia 2010,* Ristek, LIPI, ITB, PU, Bandung, 1 Juli 2010

[2] Atkinson, G. M., & Boore, D. M. 2003. Empirical Ground-Motion Relations for Subduction-Zone Earthquakes and Their Application to Cascadia and Other Regions. Society, 93(4), 1703-1729.

[3] Campbell, K. W. 2003. Prediction of Strong Ground Motion Using the Hybrid Empirical Method and Its Use in the Development of Ground-Motion (Attenuation) Relations in Eastern North America. Society, 93(3), 1012-1033.

[4] Megawati, K., & Pan, T. Chien. 2010. Ground-motion attenuation relationship for the Sumatran megathrust earthquakes. Earthquake engineering Structural Dynamic. (39) 827-845. doi:10.1002/eqe

[5] Irsyam, M., et.al., 2008. Proposed seismic hazard maps of Sumatra and Java islands and microzonation study of Jakarta city Indonesia. Journal Earth System Science, (November), 865-878.

[6] Zera Tati, et.al., 2017. *Comparison of Three Models Peak Ground Acceleration (PGA) in Bengkulu, Indonesia,* IOSR Journal of Applied Geology and Geophysics (IOSR-JAGG). 5. (1). 31-36. doi : 10.9790/0990-0501013136

[7] Keisuke Himoto, et.al, 2014. Analysis of Ignitions Following 2011 Tohoku Earthquake Using Kawasumi Model, Fire Safety Science-Proceedings of The Eleventh International Symposium pp.704-717, 2014, doi: 10.3801/iafss.fss.11-704

[8] Zera Tati, M Ocky. 2016. Pemetaan Nilai Percepatan Tanah Maksimum (PGA) Berdasarkan Model Kawashumi dan Hasil pengukuran Accelerograph Stasiun Cilacap. Jurnal Al- Fiziya. (9). 2. 116-124.

[9] Widodo, P, 2012. Seismologi Teknik & Rekayasa Kegempaan. Yogyakarta, Pustaka Pelajar.

[10] Sieh K, Natawidjaja D, 2000. Neotectonics of the Sumatran fault, Indonesia, Journal of Geophysical Research Solid Earth. (105). B12. https://doi.org/10.1029/2000JB900120

Available online at:
Al-Fiziya: Journal of Materials Science, Geophysics, Instrumentation and Theoretical Physics
Website: http://journal.uinjkt.ac.id/index.php/al-fiziya
Vol.4 No. 2 Tahun 2021, 89 -94

Improved Steepest Descent Method using Modified Bessel Function $K_{1/4}$ for Gamma Function Evaluation

Adam B. Cahaya [1,†]

[1]Department of Physics, Faculty of Mathematics and Natural Sciences, Universitas Indonesia
Depok 16424, Indonesia

[†]adam@sci.ui.ac .id

Submitted : July 2021; Revised : December 2021; Approved : December 2021; Available Online : December 2021

Abstrak. Metode *Steepest descent* (turunan tercuram menggunakan aproksimasi fungsi Gaussian $Ae^{-B(x-C)^2}$ketika memperkirakan nilai integral dari sebuah fungsi. Dalam artickel ini kami meningkatkan aproksimasi ini dengan menggunakan fungsi berbentuk $Ae^{-B(x-C)^2-D(x-C)^4}$. Sebagai contoh, kami melakukan aproksimasi terhadap nilai fungsi gamma untuk mendapatkan aproksimasi yang lebih baik daripada Stirling formula yang sering digunakan untuk estimasi nilai faktorial dari bilangan besar.

***Kata Kunci**: metode Steepest descent, formula Stirling, fungsi gamma..*

Abstract. Steepest descent method employs a Gaussian function $Ae^{-B(x-C)^2}$ when approximating an integral of a function. In this article we improve the approximation by using function in the form of $Ae^{-B(x-C)^2-D(x-C)^4}$. As an example, we approximate the value of gamma function to provide improved approximation for Stirling formula that is often used for estimating factorial of a large number.

***Keywords**: Steepest descent method, Stirling formula, gamma function.*

DOI : *10.15408/fiziya.v4i2.21843*

P-ISSN: 2621-0215, E-ISSN: 2621-489X

INTRODUCTION

Factorial of a positive integer is defined as the following product.

$$n! = n \times (n-1) \times (n-2) \times \cdots \times 2 \times 1 \quad (1)$$

This definition can be extended to complex and real number by using gamma function.

$$z! = \Gamma(z+1) = \int_0^\infty t^z e^{-t} dt \quad (2)$$

The evaluation of the factorial of a large number by calculating the product of positive integers require a very long time. The most used formula for approximation of the large factorials is the following Stirling's formula

$$n! \approx \sqrt{2\pi} n^{n+\frac{1}{2}} e^{-n} \quad (3)$$

Slightly better approximation formulas have also been developed [1].

$$n! \approx \sqrt{2\pi}(n+p)^{n+\frac{1}{2}} e^{-(n+p)}, \quad (4)$$

Where p is constant. In particular, $p = 0$ corresponds to Stirling formula, while $p = \frac{1}{2}$ and $\frac{1}{2} \pm \frac{1}{\sqrt{12}}$ are also known as Burnside's formula [2] and Schuster formula [3], respectively. Eq. (4) can be derived by approximating $t^z e^{-t}$ inside the integral expression of gamma function using steepest descent method [4] , as illustrated in Fig. 1.

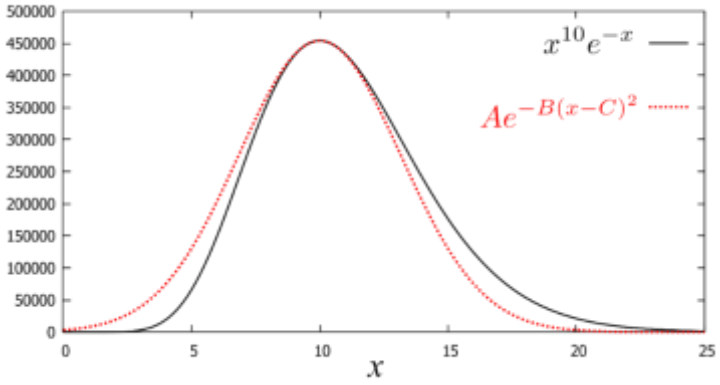

Figure 1. Approximation of $10! = \int_0^\infty x^{10} e^{-x}\, dx$ using $\int_{-\infty}^{\infty} Ae^{-B(x-C)^2}\, dx$

In the steepest descent method, $t^z e^{-t}$ function is approximated using Gaussian function in the form of $Ae^{-B(x-C)^2}$. While the steepest descent is one of the simplest and best known methods for approximating a function[5], [6], how to improve this method is still an ongoing research question[7], [8]. In this article we show that the Steepest descent method can be improved by using higher order exponential function $Ae^{-B(x-C)^2-D(x-C)^2}$. In particular, we demonstrate that a better approximation than Stirling formula can be obtained by approximating the expression for gamma function for a large number with $Ae^{-B(x-C)^2-D(x-C)^2}$.

METHODS

Approximation using $Ae^{-B(x-C)^2}$ and $Ae^{-B(x-C)^2-D(x-C)^2}$

Let us first discuss the steepest descent approximation for generalized Stirling formula (Eq. 4). By using variable substitution $t = x^m$, gamma function in Eq. (2) can be written in the following integral

$$n! = m\int_0^\infty x^{mn+m-1}e^{-x^m}\,dx = \int_0^\infty e^{\log m+(mn+m-1)\log x-x^m}\,dx. \tag{5}$$

In the steepest descent, this integral can be evaluated by taking the Taylor expansion of the function inside the exponential

$$\log m + (mn+m-1)\log x - x^m = \log A - B(x-C)^2 + O((x-C)^3), \tag{6}$$

where

$$A = m\left(n+1-\frac{1}{m}\right)^{\left(n+1-\frac{1}{m}\right)} e^{-\left(n+1-\frac{1}{m}\right)}, \tag{7a}$$

$$B = \frac{m^2}{2}\left(n+1-\frac{1}{m}\right)^{1-\frac{2}{m}}, \tag{7b}$$

$$C = \left(n+1-\frac{1}{m}\right)^{\frac{1}{m}}. \tag{7c}$$

By ignoring $O((x-C)^3)$ we can approximate the integral using the following equation.

$$\int_{-C}^{\infty} e^{-Bx^2}dx \approx \int_{-\infty}^{\infty} e^{-Bx^2}\,dx = \sqrt{2\pi}\left(n+1-\frac{1}{m}\right)^{n+\frac{1}{2}} e^{-\left(n+1-\frac{1}{m}\right)} \tag{8}$$

One can see that Eqs. (3) and (4) are obtained when $m = 1$ and $(1-p)^{-1}$, respectively.

This approximation can be improved by choosing $m = 3$. In this case the expansion coefficient of $(x-C)^3$ is zero and we can approximate the function into higher order, as illustrated in Fig. 2.

$$\log 3 + (3n+2)\log x - x^3 = \log A - B(x-C)^2 - D(x-C)^4 + O((x-C)^5) \tag{9}$$

where

$$A_{m=3} = 3\left(n+\frac{2}{3}\right)^{\left(n+\frac{2}{3}\right)} e^{-\left(n+\frac{2}{3}\right)} \tag{10a}$$

$$B_{m=3} = \frac{9}{2}\left(n+\frac{2}{3}\right)^{\frac{1}{3}} \tag{10b}$$

$$C_{m=3} = \left(n+\frac{2}{3}\right)^{\frac{1}{3}} \tag{10c}$$

$$D = \frac{3}{4}\left(n+\frac{2}{3}\right)^{-\frac{1}{3}} \tag{10d}$$

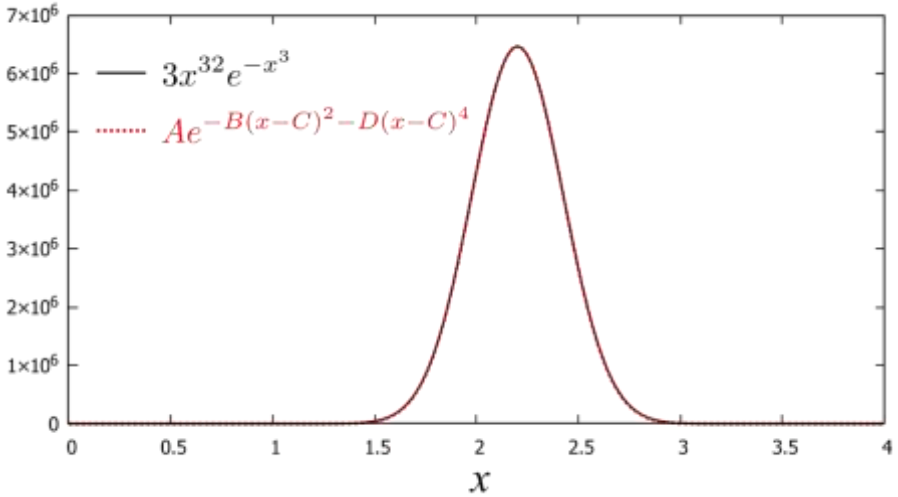

Figure 2. Approximation of $10! = 3\int_0^\infty x^{32}e^{-x^3}\,dx$ using $\int_{-\infty}^{\infty} Ae^{-B(x-C)^2-D(x-C)^4}\,dx$

In this case, we can approximate the integral using the following equation.

$$\int_{-C}^{\infty} e^{-Bx^2-Dx^4}dx \approx \int_{-\infty}^{\infty} e^{-Bx^2-Dx^4}dx = \frac{1}{2}\sqrt{\frac{B}{D}}e^{\frac{B^2}{8D}}K_{\frac{1}{4}}\left(\frac{B^2}{8D}\right) \tag{11}$$

Here $K_\alpha(x)$ is the modified Bessel function of the second kind, which is defined as follows

$$K_\alpha(x) = \int_0^{\infty} e^{-x\cosh t}\cosh \alpha t\, dt \tag{12}$$

The asymptotic form of $K_\alpha(x)$ for large x is[9], [10]

$$K_\alpha(x) = \sqrt{\frac{\pi}{2x}}e^{-x}\left(1 + \frac{4\alpha^2-1}{8x} + \frac{(4\alpha^2-1)(4\alpha^2-3^2)}{2!\,(8x)^2} + \frac{(4\alpha^2-1)(4\alpha^2-3^2)(4\alpha^2-5^2)}{3!\,(8x)^3} + \cdots\right) \tag{13}$$

Therefore

$$\int_{-\infty}^{\infty} e^{-Bx^2-Dx^4}dx = \sqrt{\frac{\pi}{B}}\left(1 + \frac{\frac{1}{4}-1}{B^2}D + \frac{\left(\frac{1}{4}-1\right)\left(\frac{1}{4}-3^2\right)}{2!\,B^4}D^2 + \frac{\left(\frac{1}{4}-1\right)\left(\frac{1}{4}-3^2\right)\left(\frac{1}{4}-5^2\right)}{3!\,B^6}D^3 + \cdots\right) \tag{14}$$

RESULT AND DISCUSSION

We can improve the generalized Stirling formula by using $Ae^{-B(x-C)^2-D(x-C)^4}$ to approximate function inside the integral expression for gamma function. By substituting Eqs. (10a)-(10d), we can arrive at the following improved approximation.

$$n! \approx 3\left(n+\frac{2}{3}\right)^{n+1}e^{-\left(n+\frac{2}{3}\right)}\frac{\sqrt{6}}{2}e^{\frac{27}{8}\left(n+\frac{2}{3}\right)}K_{\frac{1}{4}}\left(\frac{27}{8}\left(n+\frac{2}{3}\right)\right) \tag{15}$$

Furthermore, we can use the asymptotic form of $K_\alpha(x)$ to estimate the corrections

$$= \left(n+\frac{2}{3}\right)^{n+\frac{1}{2}}e^{-\left(n+\frac{2}{3}\right)}\sqrt{2\pi}\left(1 + \frac{\frac{1}{4}-1}{27\left(n+\frac{2}{3}\right)} + \frac{\left(\frac{1}{4}-1\right)\left(\frac{1}{4}-3^2\right)}{2!\,27^2\left(n+\frac{2}{3}\right)^2} + \frac{\left(\frac{1}{4}-1\right)\left(\frac{1}{4}-3^2\right)\left(\frac{1}{4}-5^2\right)}{3!\,27^3\left(n+\frac{2}{3}\right)^3} + \cdots\right) \tag{16}$$

The accuracy of this approximation is illustrated in the Table 1.

Table 1 Accuracy of approximation

n	$n!$	$\sqrt{2\pi}n^{n+\frac{1}{2}}e^{-n}$	$\left(n+\frac{2}{3}\right)^{n+\frac{1}{2}}e^{-\left(n+\frac{2}{3}\right)}\sqrt{2\pi}\left(1+\frac{\frac{1}{4}-1}{27\left(n+\frac{2}{3}\right)}+\cdots\right)$	**Deviation (%)**

1	1	0.92	1.00	0.202%
2	2	1.92	2.00	0.199%
4	24	23.51	23.96	0.148%
8	40320	39902.40	40283.02	0.092%
10	3.629×10^{6}	3.599×10^{6}	3.626×10^{6}	0.077%
20	2.433×10^{18}	2.423×10^{18}	2.432×10^{18}	0.042%
40	8.159×10^{47}	8.142×10^{47}	8.157×10^{47}	0.022%
80	7.157×10^{118}	7.149×10^{118}	7.156×10^{118}	0.011%
100	9.333×10^{157}	9.325×10^{157}	9.332×10^{157}	0.009%

Here we note that $O((x-C)^5)$ terms in Eq. (18) can be included for better approximation by expansion of $e^{O((x-C)^5)}$ and utilize the following relations.

$$\int_{-\infty}^{\infty} e^{-Bx^2-Dx^4}\,x^{4s}dx = (-1)^s\sqrt{\frac{\pi}{B}}\frac{\partial^s}{\partial D^s}\left(1+\frac{\frac{1}{4}-1}{B^2}D+\frac{\left(\frac{1}{4}-1\right)\left(\frac{1}{4}-3^2\right)}{2!\,B^4}D^2 + \frac{\left(\frac{1}{4}-1\right)\left(\frac{1}{4}-3^2\right)\left(\frac{1}{4}-5^2\right)}{3!\,B^6}D^3+\cdots\right) \tag{16a}$$

$$\int_{-\infty}^{\infty} e^{-Bx^2-Dx^4}\,x^{4s+2}dx = (-1)^{s+1}\frac{\partial}{\partial B}\sqrt{\frac{\pi}{B}}\frac{\partial^s}{\partial D^s}\left(1+\frac{\frac{1}{4}-1}{B^2}D+\frac{\left(\frac{1}{4}-1\right)\left(\frac{1}{4}-3^2\right)}{2!\,B^4}D^2 + \frac{\left(\frac{1}{4}-1\right)\left(\frac{1}{4}-3^2\right)\left(\frac{1}{4}-5^2\right)}{3!\,B^6}D^3+\cdots\right) \tag{16b}$$

CONCLUSION

To summarize, we review the derivation of Stirling formula by using steepest descent method for approximating gamma function. We can arrive at the Stirling approximation and other and related formulas by substituting the appropriate m into Eq. (8).

Table 2. Values of m for Stirling-like approximations

m	**Formula**
1	Stirling formula $\sqrt{2\pi}n^{n+\frac{1}{2}}e^{-n}$
2	Burnside formula $\sqrt{2\pi}\left(n+\frac{1}{2}\right)^{n+\frac{1}{2}}e^{-\left(n+\frac{1}{2}\right)}$

	Schuster formula
$\frac{2\sqrt{3}}{\sqrt{3}\mp 1}$	$\sqrt{2\pi}e^{-\left(n+\frac{1}{2}\pm\frac{1}{\sqrt{12}}\right)}\left(n+\frac{1}{2}\pm\frac{1}{\sqrt{12}}\right)^{n+\frac{1}{2}}$
$\frac{1}{1-p}$	$\sqrt{2\pi}(n+p)^{n+\frac{1}{2}}e^{-(n+p)}$

We show that we can improve the steepest descent approximation by replacing Gaussian function $Ae^{-B(x-C)^2}$ with higher exponential term $Ae^{-B(x-C)^2-D(x-C)^4}$. By applying the improved method to integral expression of gamma function, we can arrive at the improved Stirling approximation that utilize modified Bessel function of the second kind $K_{1/4}$ (see Eq. 15). The accuracy of this approximation can be seen in the Table 1.

REFERENCES

[1] W. A. Bowers, "More about approximations to n!," *Am. J. Phys.*, vol. 51, no. 9, p. 778, Sep. 1983, doi: 10.1119/1.13141.

[2] W. Burnside, "A rapidly convergent series for log N," *Messenger Math*, vol. 46, no. 1, pp. 157–159, 1917.

[3] W. Schuster, "Improving Stirling's formula," *Arch. der Math.*, vol. 77, pp. 170–176, 2001.

[4] C. Leubner, "Generalised Stirling approximations to N!," *Eur. J. Phys.*, vol. 6, no. 4, pp. 299–301, Oct. 1985, doi: 10.1088/0143-0807/6/4/016.

[5] S. S. Petrova and A. D. Solov'ev, "The Origin of the Method of Steepest Descent," *Hist. Math.*, vol. 24, no. 4, pp. 361–375, 1997, doi: https://doi.org/10.1006/hmat.1996.2146.

[6] J. C. Meza, "Steepest descent," *WIREs Comput. Stat.*, vol. 2, no. 6, pp. 719–722, 2010, doi: https://doi.org/10.1002/wics.117.

[7] Y. Pu and J. Wang, "Fractional-order global optimal backpropagation machine trained by an improved fractional-order steepest descent method," *Front. Inf. Technol. Electron. Eng.*, vol. 21, no. 6, pp. 809–833, 2020, doi: 10.1631/FITEE.1900593.

[8] J.-C. Son, M.-K. Baek, S.-H. Park, and D.-K. Lim, "Improved Immune Algorithm Combined with Steepest Descent Method for Optimal Design of IPMSM for FCEV Traction Motor," *Energies*, vol. 14, no. 13, 2021, doi: 10.3390/en14133904.

[9] E. J. Weniger and J. Cížek, "Rational approximations for the modified Bessel function of the second kind," *Comput. Phys. Commun.*, vol. 59, no. 3, pp. 471–493, 1990, doi: https://doi.org/10.1016/0010-4655(90)90089-J.

[10] Z.-H. Yang and Y.-M. Chu, "On approximating the modified Bessel function of the second kind," *J. Inequalities Appl.*, vol. 2017, no. 1, p. 41, 2017, doi: 10.1186/s13660-017-1317-z.

Available online at:
Al-Fiziya: Journal of Materials Science, Geophysics, Instrumentation and Theoretical Physics
Website: http://journal.uinjkt.ac.id/index.php/al-fiziya
Vol. 4 No. 2 Tahun 2021, 95 - 103

Quantum Ericson Engine with Multiple States in One Dimensional Potential Well

Nailul Hasan [1,†]

[1]Program Studi Teknik Industri, Fakultas Teknik, UPN "Veteran" UPN Jatim Fisika FST
Jl. Rungkut Madya No.1, Gn. Anyar, Kec. Gn. Anyar, Kota SBY, Jawa Timur 60294

[†]nailul.hasan.fisika@upnjatim.ac.id

Submitted : August 2021; Revised : October 2021; Approved : December 2021; Available Online : December 2021

Abstrak. Sebuah mesin kuantum ericson yang terdiri dari satu partikel dengan banyak keadaan, telah dieksplorasi. Ini adalah analogi kuantum untuk mesin ericson klasik yang terdiri dari kombinasi dua proses isotermal dan dua proses isobarik. Dengan menganalogikan partikel dalam potensial tak terbatas satu dimensi serta gas dalam silinder piston, proses termodinamika kuantum dalam mesin ericson kuantum dapat dijelaskan dari analogi proses klasik seperti isotermal, dan isobarik. Hasil penelitian menunjukkan bahwa efisiensi termal mesin ericson kuantum memiliki kemiripan dengan mesin ericson klasik.ta.

***Kata Kunci**: mesin ericson, mesin kuantum ericson, proses isotermal, proses isobarik*

Abstract. It has been investigated a quantum ericson-engine consisting of a single particle with numerous states. It's a quantum equivalent of the classical Ericson engine, which is made up of two isothermal and two isobaric processes. Quantum thermodynamic processes in a quantum ericson-engine can be explained using analogies of classical processes such as isothermal and isobaric by comparing a particle in a one-dimensional infinite potential well to a gas in a piston-cylinder. According to the findings, the thermal efficiency of the quantum ericson-engine is comparable to that of the classical ericson-engine.

***Keywords**: ericson engine, quantum ericson-engine, isothermal process, isobaric process*

DOI : *10.15408/fiziya.v4i2.22169*

P-ISSN: 2621-0215, E-ISSN: 2621-489X

INTRODUCTION

A heat engine is a machine that can transform heat energy into mechanical energy. Heat energy cannot be turned totally into work in a cycle, according to the second rule of thermodynamics. The thermal efficiency of a heat engine is defined as the ratio of work to heat energy entering the heat engine. In general, the efficiency of a traditional heat engine is greater than 50%. It means that no traditional heat engine, even the basic dual-engine, can convert all of the heat energy flowing into the system into work [1, 2]. Bender et al. successfully constructed a quantum heat engine in the form of a single particle in a one-dimensional infinite potential well, indicating the presence of a quantum heat engine. A gas system in a piston tube is analogous to this arrangement [3]. Bender's research was successful in articulating the efficiency of the quantum Carnot engine, paving the way for further quantum heat engine research. [4, 5, 6, 7, 8, 9, 10, 11, 12, 13, 14].

A single particle trapped in a one-dimensional infinite potential well with one wall can move freely like a piston in this research, which looks at the quantum ericson-engine using a comparable setup. It is necessary to determine the quantum ericson-engine efficiency formulation and compare it to the classical version [15]. This study is likely to pave the way for more quantum mechanics-based research, particularly in the realm of quantum ericson engines.

Our paper is organized as follows: at first, we define quantum isochoric and isothermal processes based on quantum identification of work performed and heat exchange. Second, we study the cycle of the quantum stirling engine, then we discuss the efficiency and compare it with the classical stirling engine. At last, we make a short discussion according to the topic.

RESEARCH METHOD

A single particle having mass m obeys non-relativistic wave equation, so called schrodinger equation. The particle is confined in a one dimensional box of width L with infinite potential walls.

$$-\frac{\hbar^2}{2\mathrm{m}}\frac{\partial^2\varphi}{\partial \mathrm{x}^2} = \mathrm{E}\varphi$$

Or we can rewrite it

$$\frac{\partial^2\varphi}{\partial \mathrm{x}^2} = -\frac{2\mathrm{mE}}{\hbar^2}\varphi = -\mathrm{k}^2\varphi$$

Or where the constant is $\mathrm{k}^2 = \frac{2\mathrm{mE}}{\hbar^2}$. It is related to energy of particle $\mathrm{E} = \frac{\mathrm{k}^2\hbar^2}{2\mathrm{m}}$. The solution of the equation is

Vol. 4 No. 2 Tahun 2021, 95 - 103
P-ISSN: 2621-0215, E-ISSN: 2621-489X

$$\varphi(x) = A \sin \sin kx + B \cos \cos kx$$

The value B from boundary condition of wave function, $\varphi(0) = B = 0$. The other end $\varphi(L) = A \sin \sin kL = 0$ make the value

$$kL = n\pi$$

Where quantum number n=1,2,3,4, ...ect. The energy of particle now is quantized

$$E_n = \frac{n^2\pi^2\hbar^2}{2mL^2}$$

The value A can be derived from normalization conditions for the wave function.

$$\varphi_n(x) = \sqrt{\frac{2}{L}} \sin \sin \frac{n\pi}{L}x$$

The absolute square of the wave function tells us the probability density of the particle for a given quantum number n. The general solution for the equation is just linear combination for every possible solution

$$\psi(x) = \sum_{n=1}^{\infty} a_n\varphi_n(x)$$

The total energy of the system is given by

$$E = \sum_{n=1}^{\infty} |a_n|^2 E_n$$

Where $|a_n|^2$ tell us about the probability of the particle in state n and energy E_n. The Normalization condition for wave function give us

$$\sum_{n=1}^{\infty} |a_n|^2 = 1$$

The force exerted by the particle to the wall is given by

$$F = -\frac{\partial E}{\partial L} = \sum_{n=1}^{\infty} |a_n|^2 \frac{\pi^2\hbar^2}{mL^3}$$

As the opposite, the work of the the force can be calculated by equation

$$W = \int FdL$$

As in the classical, the quantum stirling engine we have two isothermal processes and two isochoric processes. From the figure, the process AB is isothermal where energy

Vol. 4 No. 2 Tahun 2021, 95 - 103
P-ISSN: 2621-0215, E-ISSN: 2621-489X

is constant with heat added equal to the work by the system. BC is isochoric or isovolume Constant force from state. The process CD is isothermal where energy is constant with heat added equal to the work by the system. DA is isochoric or isovolume Constant force from state.

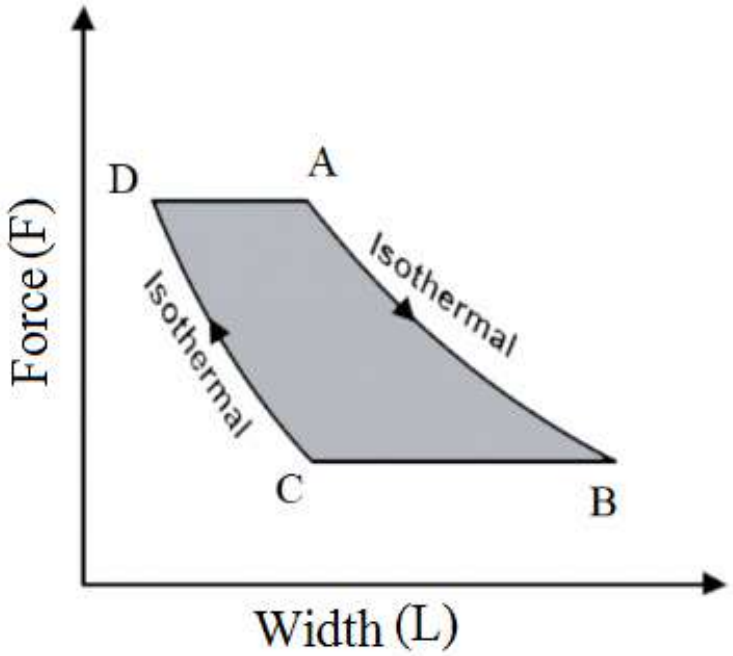

Figure 1. Cycle for Ericson Engine consist two Isothermal processes and two Isobaric processes. In The system Force is acting as pressure and width is acting as volume.

The process AB is isothermal energy is constant which heat added equal to the work by the system. The transition from n=1 to the superposition state 1, 2, 3, 4,…., N. The wave function is superposition of the state

$$\frac{\pi^2\hbar^2}{2mL_A^2} = E_A$$

$$\psi_{AB}(x) = \sum_{n=1}^{N} a_n \varphi_n(x)$$

With normalization condition of the wave function, $\sum_{n=1}^{N} |a_n|^2 = 1$

The energy is give by

$$E_{AB} = \sum_{n=1}^{N} |a_n|^2 n^2 \frac{\pi^2\hbar^2}{2mL^2} = E_A$$

$$s_{Bf}\frac{\pi^2\hbar^2}{2mL_B^2} = \frac{\pi^2\hbar^2}{2mL_A^2}$$

$$s_{Bf}L_A^2 = L_B^2$$

Where the coefficient $s_{AB} = \sum_{n=1}^{N} |a_n(L)|^2 n$, $s_{Bf} = \sum_{n=1}^{N} |a_n(L_B)|^2 n$
The force

$$F_{AB} = s_{AB} \frac{\pi^2 \hbar^2}{mL^3} = \frac{2E_A}{L}$$

The change in energy is same as heat added the system.

$$Q_{AB} = W_{AB} = \int_{L_A}^{L_B} F_{AB} dL = 2E_A \ln\left(\frac{L_B}{L_A}\right)$$

Where the energy change in this process, $\Delta E_{AB} = 0$

BC is isobaric

$$\psi_{BC}(x) = \sum_{n=1}^{N} a_n \varphi_n(x)$$

Constant force from state. The energy is given by

$$E_{BC} = s_{BC} \frac{\pi^2 \hbar^2}{2mL^2}$$

$s_{BC} = \sum_{n=1}^{N} |a_n(L)|^2 n$. The force can be derived from the energy,

$$F_{BC} = s_{BC} \frac{\pi^2 \hbar^2}{mL^3}$$

Constant force give us relation

$$\frac{s_{Cf} \pi^2 \hbar^2}{mL_C^3} = \frac{s_{Bf} \pi^2 \hbar^2}{mL_B^3}$$
$$s_{Cf} L_B^3 = s_{Bf} L_C^3$$

The work done to the system

$$W_{BC} = \int_{L_B}^{L_C} F_{CA} dL = \int_{L_B}^{L_C} \frac{s_{Cf} \pi^2 \hbar^2}{mL_C^3} dL = \frac{s_{Cf} \pi c \hbar}{L_C^2} (L_C - L_B)$$
$$= \frac{s_{Cf} \pi^2 \hbar^2}{mL_C^2} - \frac{\pi^2 \hbar^2}{mL_A^2}$$

The energy change

$$\Delta E_{BC} = E_C - E_B = \frac{s_{Cf} \pi^2 \hbar^2}{2mL_C^2} - \frac{s_{Bf} \pi^2 \hbar^2}{2mL_B^2} = \frac{s_{Cf} \pi^2 \hbar^2}{2mL_C^2} - \frac{\pi^2 \hbar^2}{2mL_A^2}$$

Heat energy can be derived from the law of conservation energy.

$$Q_{BC} = \Delta E_{BC} + W_{BC} = \frac{3s_{Cf}\pi^2\hbar^2}{2mL_C^2} - \frac{3\pi^2\hbar^2}{2mL_A^2}$$

The process CD is isothermal energy is constant which heat added equal to the work by the system. The transition from to the superposition state 1, 2, 3, 4,…., N. The wave function is superposition of the state

$$E_C = s_{Cf}\frac{\pi^2\hbar^2}{2mL_C^2}$$

$$\psi_{CD}(x) = \sum_{n=1}^{N} a_n\varphi_n(x)$$

With normalization condition of the wave function, $\sum_{n=1}^{N}|a_n|^2 = 1$

The energy is give by

$$E_{CD} = \sum_{n=1}^{N} |a_n|^2 n^2 \frac{\pi^2\hbar^2}{2mL^2} = E_C$$

$$s_{Df}\frac{\pi^2\hbar^2}{2mL_D^2} = s_{Cf}\frac{\pi^2\hbar^2}{2mL_C^2}$$

$$s_{Df}L_C^2 = s_{Cf}L_D^2$$

Where the coefficient $s_{Df} = \sum_{n=1}^{N}|a_n(L_D)|^2 n$
The force

$$F_{CD} = s_{CDf}\frac{\pi^2\hbar^2}{mL^3} = \frac{2E_C}{L}$$

The change in energy is the same as heat added to the system.

$$Q_{CD} = W_{CD} = \int_{L_C}^{L_D} F_{AB}dL = 2E_C \ln\left(\frac{L_D}{L_C}\right)$$

Where the energy change in this process, $\Delta E_{CD} = 0$

DA is isobaric

$$\psi_{DA}(x) = \sum_{n=1}^{N} a_n \varphi_n(x)$$

Constant force from state The energy is given by

$$E_{DA} = s_{DA} \frac{\pi^2 \hbar^2}{2mL^2}$$

$s_{DA} = \sum_{n=1}^{N} |a_n|^2 n$. The force can be derived from the energy,

$$F_{DA} = s_{DA} \frac{\pi^2 \hbar^2}{mL^3}$$

Constant pressure give us relation

$$\frac{s_{Df} \pi^2 \hbar^2}{mL_D^3} = \frac{\pi^2 \hbar^2}{mL_A^3}$$

$$L_D^3 = L_A^3 s_{Df}$$

The work done to the system

$$W_{DA} = \int_{L_D}^{L_A} F_{DA} dL = \int_{L_D}^{L_A} \frac{s_{Df} \pi^2 \hbar^2}{mL_D^3} dL = \frac{s_{Df} \pi^2 \hbar^2}{mL_D^3} (L_A - L_D)$$
$$= \frac{\pi^2 \hbar^2}{mL_A^2} - \frac{s_{Df} \pi^2 \hbar^2}{mL_D^2}$$

The energy change

$$\Delta E_{DA} = E_A - E_D = \frac{\pi^2 \hbar^2}{2mL_A^2} - \frac{s_{Df} \pi^2 \hbar^2}{2mL_D^2}$$

Heat energy can be derived from the law of conservation energy.

$$Q_{DA} = \Delta E_{DA} + W_{DA} = \frac{3\pi^2 \hbar^2}{2mL_A^2} - \frac{3 s_{Df} \pi^2 \hbar^2}{2mL_D^2}$$

The net work for one cycle is just the sum of the work for each process.

$$W_{nett} = W_{AB} + W_{BC} + W_{CD} + W_{DA}$$

$$= 2E_A \ln\left(\frac{L_B}{L_A}\right) + \frac{s_{Cf} \pi^2 \hbar^2}{mL_C^2} - \frac{\pi^2 \hbar^2}{mL_A^2} + 2E_C \ln\left(\frac{L_D}{L_C}\right) + \frac{\pi^2 \hbar^2}{mL_A^2} - \frac{s_{Df} \pi^2 \hbar^2}{mL_D^2}$$
$$= 2E_A \ln\left(\frac{L_B}{L_A}\right) + 2E_C \ln\left(\frac{L_D}{L_C}\right)$$

The nett heat added to the system in only at step AB

$$Q_{in} = Q_{AB} =$$

$$\eta = 1 + \frac{Q_{CD}}{Q_{AB}} = 1 + \frac{2E_C \ln\left(\frac{L_D}{L_C}\right)}{2E_A \ln\left(\frac{L_B}{L_A}\right)} = 1 - \frac{E_C \ln\left(\frac{L_C}{L_D}\right)}{E_A \ln\left(\frac{L_B}{L_A}\right)} = 1 - \frac{E_C}{E_A}$$

We have used the fact that $\frac{L_A}{L_B} = \frac{L_D}{L_C}$

CONCLUSION

The one dimensional quantum ericson engine has the same efficiency formulation as the classical ericson engine. We have shown that the multiple-state 1D box quantum ericson Engine efficiency depends on the initial and final energy ratio of thermal compression. It is analog to the efficiency of classical ericson Engine which is determined as a ratio of the temperature of the cold and hot bath contacted, 1 because the energy, as an average, is proportional to the temperature. The width of 1D box parameter does not vary when the system is in contact with either bath. The parameter varies only during the adiabatic transitions from one bath to the other bath. This cycle may deliver work or receive work for appropriate choice of the parameter

REFERENCES

[1] M.W. Zemansky and R.D. Dittman, Heat and Thermodynamics, seventh ed (McGraw-Hill Companies, Inc, New York, 1997).
[2] T.D. Kieu, European Physical Journal D 39, 115 (2006).
[3] C.M. Bender, D.C. Brody, and B.K. Meister, Journal of Physics A: Mathematical and General 33, 4427 (2000).
[4] B.C.M. Bender, D.C. Brody, and B.K. Meister, Royal Society (2002).
[5] S. Singh, "Quantum braton engine of non-interacting fermions in one-dimensional box". arXiv preprint arXiv:1908.09281. (2019).
[6] E. Latifah and A. Purwanto, Journal of Modern Physics 02, 1366 (2011).
[7] A. Purwanto, H. Sukamto, B.A. Subagyo, and M. Taufiqi, Journal of Applied Mathematics and Physics 04, 1344 (2016).
[8] A. Purwanto, H. Sukamto, and B.A. Subagyo, Journal of Modern Physics 06, 2297 (2015).
[9] E. Latifah and A. Purwanto, Journal of Modern Physics 04, 1091 (2013).
[10] D.P. Setyo, E. Latifah, A. Hidayat, and H. Wisodo, Jurnal Penelitian Fisika Dan Aplikasinya (JPFA) 8, 25 (2018).
[11] M.S. Akbar, E. Latifah, and H. Wisodo, Journal of Physics: Conference Series 1093, (2018).

[12] H.T. Quan, Y. Liu, C.P. Sun, and F. Nori, Physical Review E 76, 1 (2007).
[13] H.T. Quan, Physical Review E - Statistical, Nonlinear, and Soft Matter Physics 79, (2009).
[14] V. Ganesan, Internal Combustion Engines, Second Edi (The McGraw-Hill Companies, New Delhi, 2003).
[15] M.J. Moran, H.N. Shapiro, D.D. Boettner, and M.B. Bailey, Fundamental of Engineering Thermodynamics, 9th edition (John Wiley and Sons, USA, 2018).

Available online at:
Al-Fiziya: Journal of Materials Science, Geophysics, Instrumentation and Theoretical Physics
Website: http://journal.uinjkt.ac.id/index.php/al-fiziya
Vol. 4 No. 2 Tahun 2021, 104 - 114

Identification of Iron Ore Deposit in Sub-Surface Using Electrical Resistivity and Induced Polarization Methods in Nangabulik, Central Kalimantan

Rizki Alpiandi [1,†], Agus Budiono [1], Yanto Sudiyanto [2], Wahyu Hidayat [2]
[1]Physics Study Program, Faculty of Sciences and Technology, State Islamic University Syarif Hidayatullah Jakarta, Ir. H. Djuanda Street No.95, Cempaka Putih, Ciputat, South Tangerang, Banten 15412, Indonesia
[2]Pusat Teknologi Pengembangan Sumberdaya Mineral (PTPSM) Badan Pengkajian dan Penerapan Teknologi (BPPT), Puspiptek Area Street, Muncul, Setu, South Tangerang, Banten 15314, Indonesia
[†]rizki.alpiandi16@mhs.uinjkt.ac.id

Submitted : August 2021; Revised : December 2021; Approved : December 2021; Available Online : December 2021

Abstrak. Nangabulik, Kabupaten Lamandau merupakan salah satu daerah di Kalimantan Tengah yang memiliki potensi akan sumberdaya mineral bijih besi. Metode yang cocok digunakan untuk menganalisis model distribusi nilai *resistivity* dan *chargeability* di bawah permukaan yang dapat menginterpretasi distribusi sebaran bijih besi dan menyelidiki keberadaan zona kemenerusan bijih besi adala metode geolistrik dan IP. Konfigurasi yang digunakan adalah *Wenner Alpha* dengan 4 lintasan yang masing-masing panjangnya 235 m. Berdasarkan hasil inversi 2D nilai *resistivity* berkisar 21,15 – 96.153,51 Ωm dan *chargeability* 23,6 – 542,58 ms. Endapan bijih besi ditemukan pada lintasan GL-01, GL-02, dan GL-04 yang ditandai dengan nilai *resistivity* 614,22 – 5.803,90 Ωm dan kontras *chargeability* berkisar 212,32 – 542,58 ms. Nilai resistivitas besar terjadi akibat adanya rongga antar fragmen bijih besi yang berbentuk kerikil – bongkah dengan butiran batuan piroklastik yang terisi udara. Berdasarkan model 3D tidak ditemukan adanya zona kemenerusan endapan bijih besi pada daerah penelitian. Jumlah endapan yang diduga sumberdaya bijih besi di daerah penelitian, pada area seluas ± 6 hektar sebesar 41.036 ton.

***Kata Kunci**: Endapan Bijih Besi, Nangabulik, Polarisasi Terinduksi, Resistivitas, Wenner Alpha*

Abstract. Nangabulik, Lamandau Regency was one of territories in Central Borneo that has potential for iron ore resources. The method that is suitable for analyzing the distribution model of the resistivity and chargeability values below the surface that can interpret the distribution of iron ore distribution and the presence of iron ore continuity zones is the geoelectric and IP method. Configuration used is Wenner Alpha with 4 passes, each of which length is 235 m. Based on the 2D inversion result, resistivity and chargeability values were 21,15 – 96.153,51 Ωm and chargeability 23,6 – 542,58 ms. Iron ore deposit is to be found at GL-01, GL-02, and GL-04 tracks marked by resistivity value 614,22 – 5.803,90 Ωm and contrast in chargeability value around 212,32 – 542,58 ms. Large resistivity value due to porous between pebble–boulder iron ore fragments shape with pyroclastic rock grains filled the air. Based on the 3D model there was not found alignment zone of iron ore deposit at the research region. Total estimated deposit iron ore resource in the research region, at area ± 6 hectares is 41.036 tons.

***Keywords**: Electrical Resistivity, Induced Polarization, Iron Ore Deposit, Nangabulik, Wenner Alpha*

DOI : *10.15408/fiziya.v4i2.21942*

P-ISSN: 2621-0215, E-ISSN: 2621-489X

INTRODUCTION

Geology of Research Area

Based on Fig. 1 Lamandau Regency is eastern part of the Sunda Shelf and borders the Barito Basin. At that time this area experienced uplift accompanied by volcanic activity which resulted in the Kuayan Formation [1]. Based on data from the Pangkalanbuun sheet, the research area is included in the pyroclastic rock unit of the Kuayan Formation (*TRvk*). This formation is composed of pyroclastic rocks (rocks resulting from ancient volcanic eruptions) with rock types of breccia, lava, tuffaceous sandstone, and tuff which are estimated to be Triassic in age and have weathered [2].

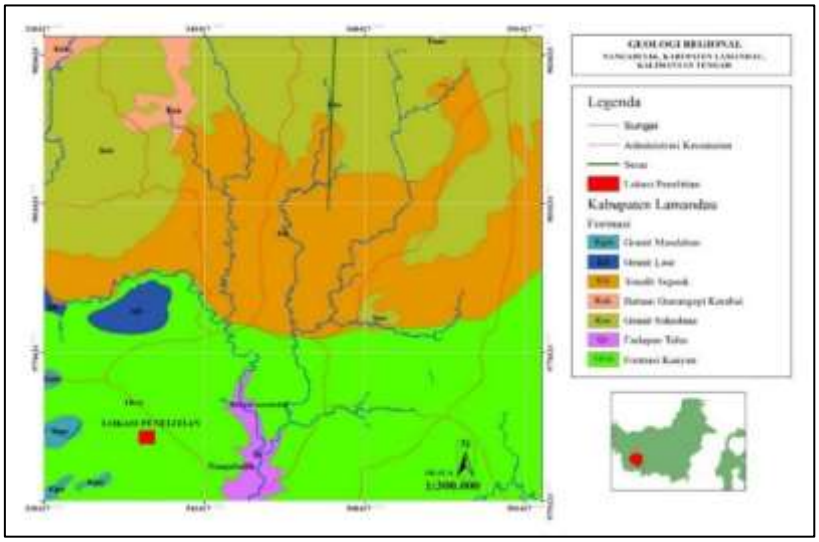

Figure. 1 Regional Geology Map of Lamandau Regency [2].

Iron Ore

Iron ore is the rock that contains iron elements or there are iron deposits in it. Economical iron deposits are generally in the form of magnetite, hematite, limonite, and siderite [3]. Iron ore deposits can be formed primary or secondary. Primary iron ore deposits can be formed by magmatic, contact metasomatic, and hydrothermal processes. Secondary iron ore deposits occur due to weathering, transportation, and sedimentation processes [4].

Laterite deposit is a type of residual deposit produced by weathering processes that occur in ultramafic-mafic rocks involving decomposition, re-deposition, and chemical accumulation. The process of weathering of ultramafic-mafic rocks is carried out intensively due to the influence of relatively small slope factors, groundwater, and weather, resulting in lateritic soils that still contain boulders of hematite and goethite iron ore in the size of granule-pebble [4].

Figure. 2 Iron Ore Fragments in Soil Layer on Any Places Forming the Lens [5].

Figure. 3 Boulders of Iron Ore are Dominated Hematite and Magnetite with weak magnetic character [5].

The results of the geological survey (Figs. 2 and 3) show the presence of lateritic iron ore deposits which are mostly hematite in the form of a sub-angular lens-angular (angled), granule-boulder formed as fragments in a clay-sand sized matrix, the result of weathering of pyroclastic rocks of the Kuayan Formation. In some places, there are fragments of magnetite iron ore with weak magnetic characteristic [5].

Electrical Resistivity

Electrical resistivity method is one of the geoelectrical methods used to investigate subsurface structures based on differences in rock resistivity. Basis of the resistivity method is Ohm's law Eq. (1).

$$V = IR \tag{1}$$

where each constant *R* is the resistance and is measured in units of when the current (*I*) is in ampere and voltage (*V*) is in volts [6].

If the parameter used to identify Ohm's Law is a certain material (copper wire) then its resistance will depend on the dimension of that material [7]. Relationship between resistance (*R*) and the dimension of a straight conductor material with length (*L*) and surface area (*A*) is:

$$\rho = R\left({}^{A}/_{L}\right) \tag{2}$$

Geoelectric measurements are usually carried out by injecting electric current (I) into the earth through two current electrodes, *C1* and *C2*, then the potential difference (*V*) that occurs is measured through two potential electrodes, *P1* and *P2* as shown in Fig. 2. The current value (*I*, unit mA) and electric potential difference (V, unit mV) are obtained so that the resistivity value (ρ_a, unit m) can be calculated using Eq. (3).

$$\rho_a = K\frac{V}{I} \tag{3}$$

where *K* is a geometric factor that depends on the arrangement of the electrodes [4].

Vol. 4 No. 2 Tahun 2021, 104 - 114
P-ISSN: 2621-0215, E-ISSN: 2621-489X

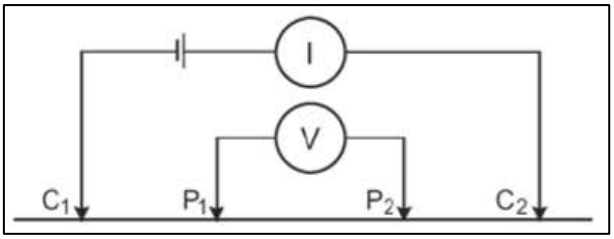

Figure. 4 Array of Four Electrodes on Geoelectric Method [4].

Induced Polarization (IP)

The phenomenon of induced polarization occurs when a current is injected and then the current is turned off. The voltage or potential that is measured after the current is turned off does not immediately become zero. The measured potential decreases slowly towards zero which is called overvoltage decay. The ratio between the voltage when the current is turned off and the voltage when the current is injected is called chargeability. Polarization is caused by two main sources namely electrode polarization and membrane polarization [3].

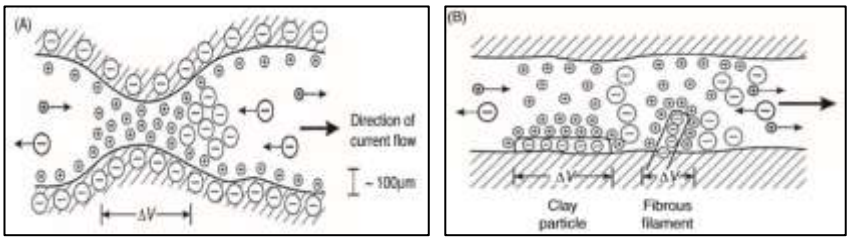

(a) (b)

Figure. 5 Membrane Polarization, (a) a constriction within a channel between mineral grains, and (b) negatively charged clay particles and fibrous elements along the sides of a channel. [3].

Based on Fig. 5a is the membrane polarization caused by the narrowing of the pores. When the current enters the pores, there is an accumulation of positive ions near the negative ions on the membrane wall. On Fig. 5b shows the membrane polarization due to the presence of clay particles in the rock pores. Clay particles containing a negative charge attract positive charges in the electrolyte solution. The negative charge scattered in the electrolyte solution will move away from the clay particles. The accumulated positive charge will inhibit the electrons originating from the injected electric current when a potential difference is given [3].

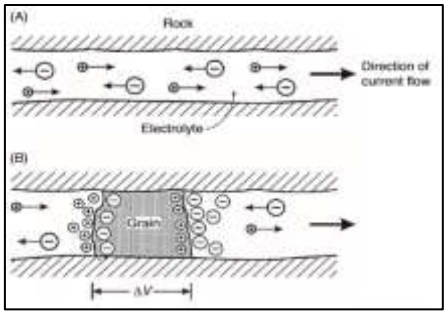

Figure. 6 Grain (electrode) polarization (a) Unrestricted electrolytic flow in an open channel (b) Polarization of an electronically conductive grain, blocking a channel [3].

Based on Fig. 6a depicts the polarization of the electrode in the pores of the rock containing the electrolyte solution. Positive ions flow in the direction of current flow. Negative ions flow in the opposite direction to the direction of current flow. In Fig. 6b describes the polarization of the electrodes in the pores of rock containing minerals. Positive and negative charges are polarized at the boundary between metallic minerals and the solution when an electric current is applied [3].

METHODS

This research was conducted in Nangabulik, Bulik District, Lamandau Regency, Central Kalimantan Province. This data is included in the area of the Mining Business Permit of PT. D. The type of configuration used is Wenner Alpha. Reason using this configuration because Wenner Alpha has low depth penetration, high sensitivity to lateral inhomogeneities, and good vertical resolution [3]. This is appropriate for identification iron ore distribution laterally and has relatively shallow depth. Geoelectric data used as many as 4 tracks with length of 235 m with a space between the electrodes of 5 m.

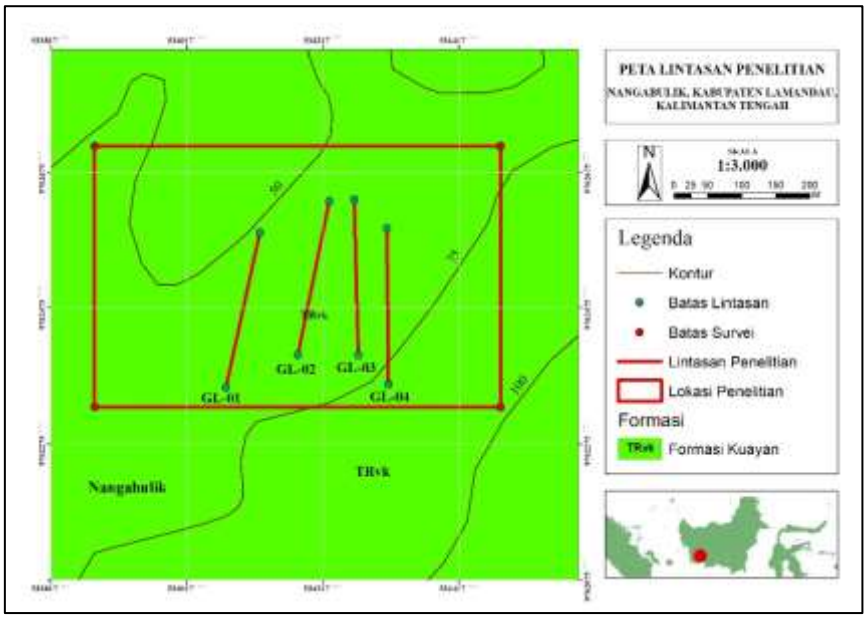

Figure. 7 Survey Tracks Design of Resistivity and Induced Polarization (IP) Methods

2D modeling of Resistivity and IP data using Res2Dinv software. This program uses the iteration method to start the initial model and try to minimize the difference between the calculated and measured resistivity and apparent chargeability values or to obtain an improved model where the calculated resistivity and apparent chargeability values are equal to or close to the measured values [6].

Then 3D modeling was carried out based on the results of 2D inversion using Geosoft Oasis Montaj software. The 3D model made is the correlation of the IP (chargeability) values of entire track so that it can be seen clearly whether or not there is a continuity zone for iron ore deposits.

Vol. 4 No. 2 Tahun 2021, 104 - 114
P-ISSN: 2621-0215, E-ISSN: 2621-489X

Process of calculating iron ore deposits in the research area using Voxler software. Volume calculations used the iso-Surface module. Iso-surface is a representation of the distribution of data values (actual chargeability) in the form of a 3D model. Estimated volume of iron ore resources is the value of the volume iso-value. The following is a research flow chart.

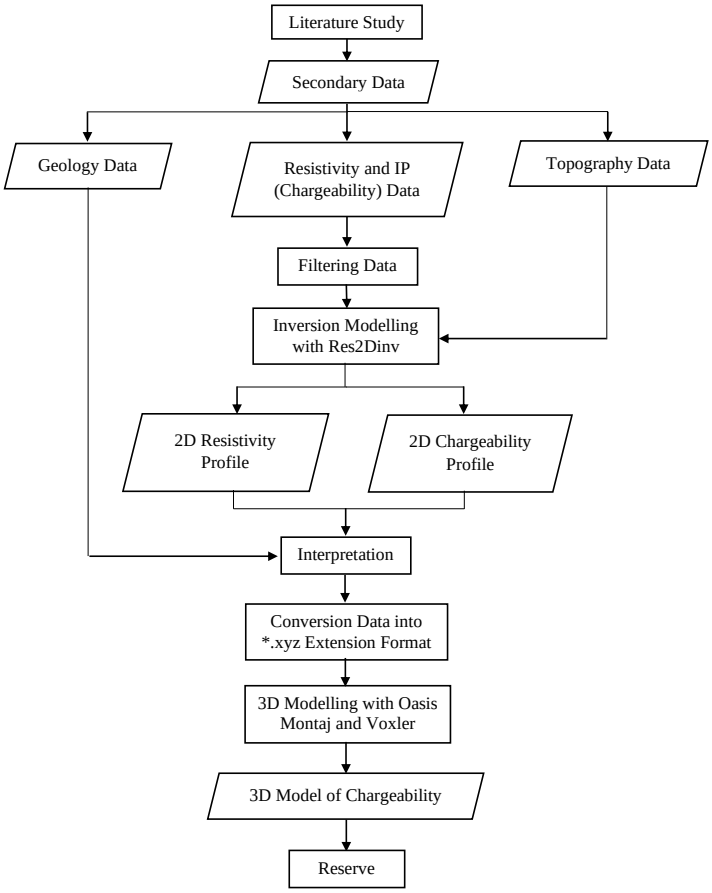

Figure. 8 Research Flow Chart

RESULTS AND DISCUSSION

Result of 2D Modelling and Interpretation

Based on result of inversion modeling obtained a 2D resistivity and induced polarization (chargeability) cross-sectional model of the entire track, then correlated with the geological data of the research area, it can be interpreted to indicate the presence of iron ore deposits on each track, as follows.

GL-01 Track

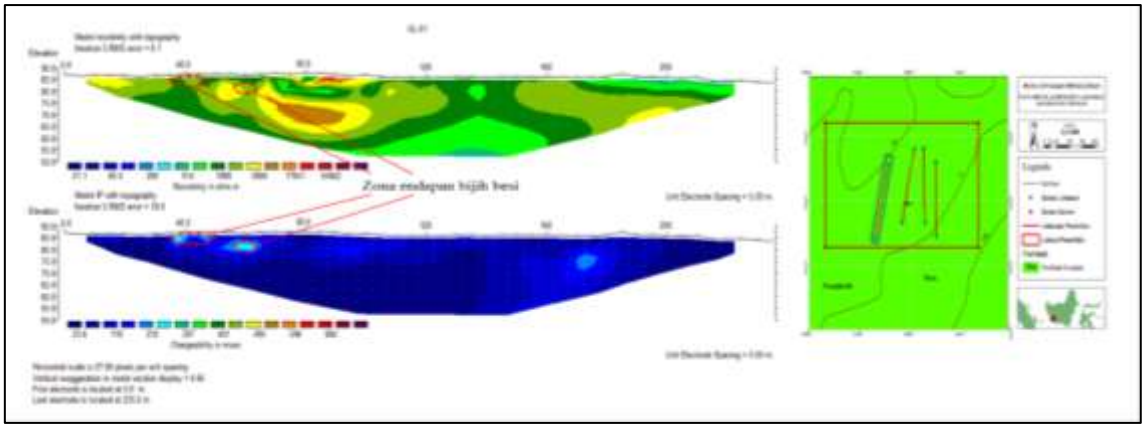

Figure. 9 Result of Inversion Modelling and Interpretation from Resistivity and Chargeability Profiles on GL-01 Track

Based on Fig. 9 obtained the resistivity value which is in the range of numbers 350,33 – 31.280,02 Ωm with the value of chargeability being in the interval of numbers 23,6 – 259,50 ms. In a 2D cross-section of chargeability, it can be seen that the chargeability value contrasts with a value range of 212,32 – 259,50 ms which is interpreted as having iron ore deposits, which correlates with a resistivity value range of 1.076,89 – 5.803,90 Ωm. So it can be seen that on the GL-01 track there are 2 iron ore deposits which are summarized in Tbl. 1.

Table. 1 Distribution of Iron Ore Deposit on GL-01 Track

Length (m)	Depth (m)	Resistivity (Ωm)	Chargeability (ms)
35 – 47,5	1,25 – 2,56	1.076,89 – 3.310,33	212,32 – 259,50
55 – 65	2,56 – 6,38	1.888,09 – 5.803,90	212,32 – 259,50

GL-02 Track

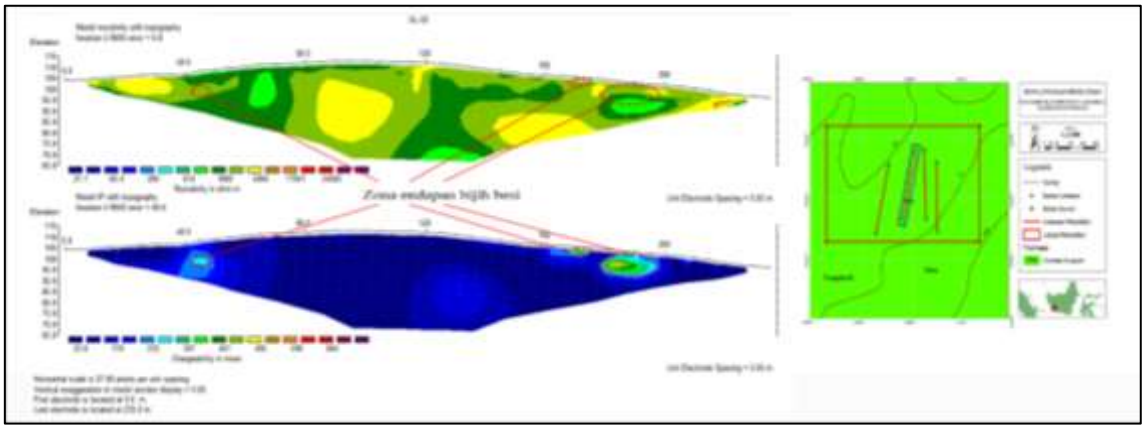

Figure. 10 Result of Inversion Modelling and Interpretation from Resistivity and Chargeability Profiles on GL-02 Track

Based on Fig. 10, resistivity value is obtained which is in interval of 614,22 – 10.175,81 Ωm with the chargeability value is in the interval of 23,6 – 542,58 ms. In the 2D cross-section of chargeability, it can be seen that the chargeability value contrasts with a value range of 212,32 – 542,58 ms which is interpreted as having iron ore deposits, which correlates with a resistivity value range of 614,22 – 5.803,90 Ωm. So it can be seen that on the GL-02 track there are 3 iron ore deposits which are summarized in Tbl. 2.

Table. 2 Distribution of Iron Ore Deposit on GL-02 Track

Length (m)	Depth (m)	Resistivity (Ωm)	Chargeability (ms)
40 – 45	6,38 – 12,4	1.888,09 – 3.310,33	212,32 – 259,50
170 – 175	1,25 – 2,56	1.888,09 – 3.310,33	212,32 – 448,22
180 – 197.5	1,25 – 9,39	614,22 – 5.803,90	212,32 – 542,58

GL-03 Track

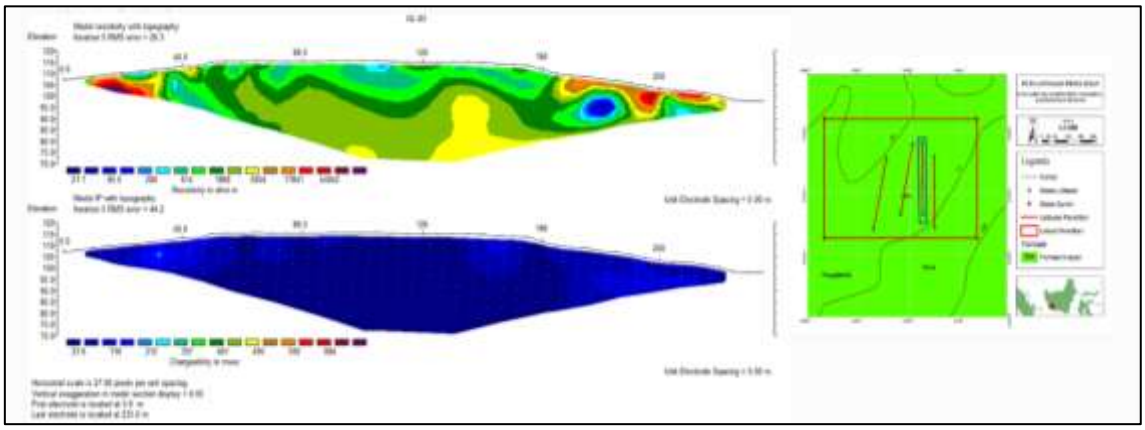

Figure. 11 Result of Inversion Modelling and Interpretation from Resistivity and Chargeability Profiles on GL-03 Track

Based on Fig. 11, resistivity value is obtained which is in the interval of 21,15 – 96.153,51 Ωm with chargeability value is in the interval of 23,6 – 212,32 ms. In 2D cross-section of chargeability, there is no contrast between the chargeability value of the iron ore deposit and the chargeability value of the surrounding rock. So it can be seen that there is no iron ore deposit on the GL-03 track.

GL-04 Track

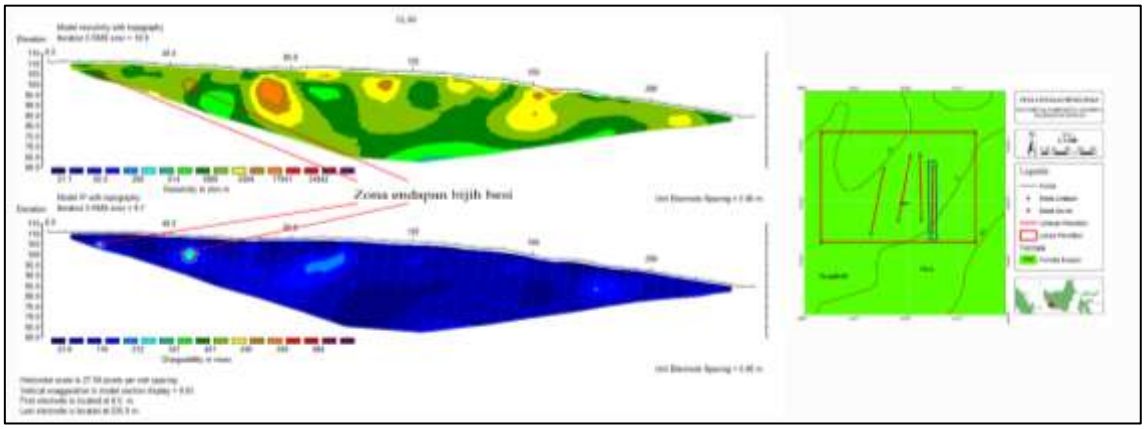

Figure. 12 Result of Inversion Modelling and Interpretation from Resistivity and Chargeability Profiles on GL-04 Track

Based on Fig. 12 obtained resistivity value which is in the interval number 350,33 – 17.840,95 Ωm with the value of chargeability is in interval number 23,6 – 306,68 ms. In the 2D cross-section of chargeability, it can be seen that the chargeability value contrasts with a value range of 212,32 – 306,68 ms which is interpreted as having iron ore deposits,

which are correlated with a resistivity value range of 1.076,89 – 3.310,33 Ωm. So it can be seen that on the GL-04 track there are 2 iron ore deposits.

Table. 3 Distribution of Iron Ore Deposit on GL-01 Track

Length (m)	Depth (m)	Resistivity (Ωm)	Chargeability (ms)
15 – 17,5	6,38 – 9,39	1.076,89 – 1.888,09	212,32 – 259,50
45 – 50	6,38 – 12,4	1.076,89 – 3.310,33	212,32 – 306,68

Resistivity value of iron ore deposits is relatively high, ranging from 614,22 Ωm, this condition is thought to occur due to the presence of cavities between iron ore fragments in the form of granule - boulders with pyroclastic rock grains filled with air, resulting in high resistivity. Generally, iron ore and other metal ores have a low resistivity range (below 100 Ωm), especially in massive iron ore bodies, not as fragments in other rock matrices.

All resistivity cross-sections in 4 geoelectric lines do not show a contrasting resistivity value range (resistivity anomaly) with the resistivity value of the surrounding rock so that in interpreting the presence of iron ore deposits below the surface it only refers to the chargeability value, where the contrast chargeability value (IP anomaly) with the chargeability value of the surrounding rock indicating the presence of iron ore below the surface ranging from 212,32 – 542,58 ms.

Distribution of Sub-Surface Iron Ore Deposits

Based on correlation of chargeability values in the form of 3D model (Fig. 13) there was no indication of a continuous zone of iron ore deposits in the study area. This is due to the location of iron ore deposits (marked by sky blue-purple) which have a chargeability value of 212,32 – 542,58 ms spread over certain locations on each track and do not show a straight line of iron ore deposits between two or more tracks.

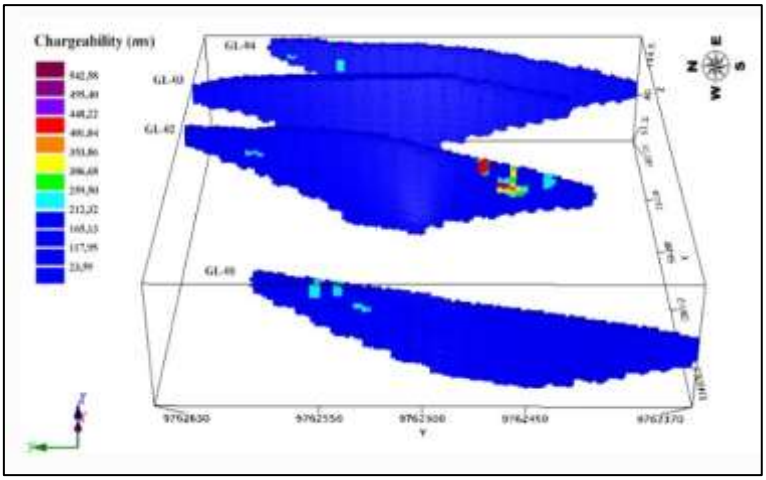

Figure. 13 3D Model Based of Inversion Result Chargeability Correlation All of Tracks

Iron Ore Reserves

Based on the results of 3D iso-surface modeling (Fig. 14) it is known that the volume of iron ore deposits in the study area within an area of ± 6 hectares is estimated to be around 10.259 m^3. This calculation is done by calculating the volume of the iron ore deposit zone which has a chargeability value of 212,32 ms. The results of the

calculation of the volume of iron ore deposits are classified as resources. If the iron ore density is assumed to be 4 g/cm^3 [8], then the ore deposit resources in an area of ± 6 hectares are as follows.

Mass = volume × density
= 10.259 m^3 × 4.000 kg/m^3
= 41.036 tons

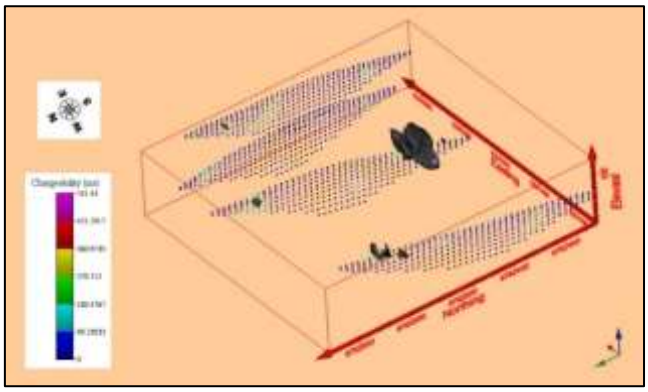

Figure 14. Distribution of Iron Ore Deposit Based of 3D Modelling Result

CONCLUSIONS

Based on results, it can be concluded that the inversion modeling of the resistivity value distribution range from 21,15 – 96.153,51 Ωm and chargeability 23,6 – 542,58 ms below the surface. Iron ore deposits in the study area are found in pyroclastic rock units of the Kuayan Formation which are indicated by resistivity values ranging from 614.22 – 5.803,90 Ωm and contrasting chargeability values ranging from 212,32 – 542,58 ms found on the GL-01 track, GL-02, and GL-04. Large resistivity value occurs due to the presence of cavities between fragments of iron ore in the form of granule-boulder with pyroclastic rock grains of clay-sand filled with air.

Result of 3D model of correlation between chargeability of the entire track, there was no indication of a continuous zone of iron ore deposits in the study area. This is due to the location of iron ore deposits scattered in certain locations on each track and does not show a straight line of iron ore deposits between two or more tracks. And resource of iron ore deposits in this research location in area of ± 6 hectares is 41.036 tons.

REFERENCES

[1] Sampurno, J. *Pendugaan Potensi Bijih Besi di Desa Bulik Kecamatan Nangabulik, Kabupaten Lamandau Kalimantan Tengah dengan Menggunakan Metode Geomagnet* (POSITRON Vol. 2, No. 1, 2012), pp. 23 – 28.
[2] Hermanto, B., dkk. *Peta Geologi Lembar Pangkalanbuun Skala 1:250.000*. Bandung: Pusat Penelitian dan Pengembangan Geologi. 1994.
[3] Reynolds, J.M. *An Introduction to Applied and Environmental Geophysics 2nd Ed*. West Sussex: Wiley-Blackwell. 2011.
[4] Sudiyanto, Y. "Pemodelan 3 Dimensi Endapan Bijih Besi Menggunakan Metoda Resistivity dan Induced Polarization (IP)" Tesis S2 Jurusan Fisika Fakultas Matematika dan Ilmu Pengetahuan Alam Universitas Indonesia. 2010.
[5] Tim PTPSM BPPT. *Survei Tinjau Potensi Bijih Besi*. Tangerang Selatan: BPPT PTPSM. 2013.

[6] Santoso B. *Kajian Nikel Laterit dengan Metode Electrical Resistivity Tomography di Daerah Batu Putih, Kolaka Utara, Sulawesi Tenggara* (Jurnal Material dan Energi Indonesia Vol. 7 No. 1 2017), pp. 24 – 30.
[7] Lowrie, W. *Fundamental of Geophysics 2nd Ed*. New York: Cambridge University Press. 2007.
[8] Candra, A., dkk. Eksplorasi Geologi Bijih Besi Berdasarkan Data Geolistrik Induksi Polarisasi Daerah Ngolonio Nusa Tenggara Timur (JIK TekMin Vol. 1, No. 2, 2015).

Available online at:
Al-Fiziya: Journal of Materials Science, Geophysics, Instrumentation and Theoretical Physics
Website: http://journal.uinjkt.ac.id/index.php/al-fiziya
Vol. 4 No. 2 Tahun 2021, 115 - 123

Design And Build Underwater Robot Control System Based On PID (Proportional Integral Derivative)

Rista [1,†], Elvan Yuniarti [1], Dewi Lestari [1]

[1]Department of Physics, Faculty of Science and Technology, Syarif Hidayatullah Islamic State University, Ir. H. Djuanda St, No.95, Cempaka Putih, Ciputat, South Tangerang, Banten 15412, Indonesia
[†]rista.rista17@mhs.uinjkt.ac.id

Submitted : November 2021; Revised : December 2021; Approved : December 2021; Available Online : December 2021

Abstrak. Indonesia memiliki perairan yang luas dan didalamnya terdapat potensi perikanan yang sangat melimpah seperti berbagai spesies ikan air tawar dan biota perairan lainnya. Besarnya peranan perairan Indonesia ini tentu perlu didukung dengan adanya sistem monitoring yang mampu mengontrol dan memantau kondisi di dalam air, seperti underwater robot. Pada penelitian ini dilakukan rancang bangun underwater robot berbasis PID (Proportional Integral Derivative). Kestabilan robot dikontrol menggunakan PID dengan feedback dari IMU MPU6050 untuk kontrol kemiringan dan feedback dari sensor tekanan MS5803 untuk kontrol posisi kedalaman. Underwater robot ini dilengkapi dengan enam buah motor DC, dimana empat buah motor DC digunakan sebagai penggerak robot pada arah vertical (ke atas dan ke bawah) sedangkan dua buah motor DC lainnya digunakan untuk menggerakn robot pada arah horizontal (maju, mundur dan berbelok). Selain itu, robot juga dilengkapi dengan dua buah lampu sebagai penerangan robot. Dalam penelitian ini, underwater robot dapat menjaga kestabilan ketika nilai parameter PID yang diberikan adalah Kp_{roll} sebesar 0.001, Ki_{roll} sebesar 0.001, Kd_{roll} sebesar 1, Kp_{pitch} sebesar 0.001, Ki_{pitch} sebesar 0.001, Kd_{pitch} sebesar 1, Kp_{depth} sebesar 5, $Ki_{depth,}$ sebesar 1 dan Kd_{depth} sebesar 1.

***Kata Kunci**: MPU6050, MS5803, PID, Underwater Robot*

Abstract. Indonesia has wide waters and in it there is very abundant fishery potential such as various species of freshwater and other aquatic biota. The large role of Indonesian waters certainly needs to be supported by a monitoring system that is able to control and monitor conditions underwater, like underwater robot. In this research, the design of an underwater robot based on PID (Proportional Integral Derivative). Robot stability is controlled using PID with feedback from IMU MPU6050 for tilt angle control and feedback from MS5803 pressure sensor for depth position control. This underwater robot is requipped with six DC motors, four DC motors are used to drive the robot in a horizontal direction (forward, backward and turn). In addition, the robot is also equipped with two lamps for lighting the robot. In this research, the underwater robot can maintain stability when given PID parameter values are 0.001 for Kp_{roll}, 0.001 for Ki_{roll}, 1 for Kd_{roll}, 0.001 for Kp_{pitch}, 0.001 for Ki_{pitch}, 1 for Kd_{pitch}, 5 for Kp_{depth}, 1 for Ki_{depth} and 1 Kd_{depth}.

***Keywords**: MPU6050, MS5803, PID, Underwater Robot*

DOI : *10.15408/fiziya.v4i2. 23173*

P-ISSN: 2621-0215, E-ISSN: 2621-489X

INTRODUCTION

Indonesia is one of the largest archipelagic countries in the world which has a strategic location. Where the area of inland waters and Indonesian archipelagic waters reaches more than 3000000 km^2, one of the types is lakes [1]. The lake is one of the waters in Indonesia which is located in a basin area and is surrounded by land. Besides having beautiful view, the lake also has abundant fishery potential such as various species of freshwater fish and other freshwater biota. The role of Indonesian waters is so large, of course it needs to be supported by a well it grated monitoring system in order to maintain the underwater ecosystem. One solution is to use an underwater robot to find out how the conditions and situations of the underwater environment area.

Underwater robot is a robot that can maneuver in water. Where this robot is usually used to make observations of underwater environmental conditions. Based on working system, underwater robots consist of two types, namely ROV (Remotely Operated Vehicle) and AUV (Autonomous Underwater Vehicle). Remotely Operated System (ROV) is an unmanned underwater robot that can maneuver in water controlled by an operator above the water surface [2]. ROVs are usually equipped with underwater positioning systems, video cameras and others according to the needs and engineering activities in the water, such as laying pipes and cables under the sea and surveying coral reefs and other marine biota [3]. Autonomous Underwater Vehicle (AUV) is an underwater robot that is autonomous, where this robot can move and carry out all activities under its own water sensors to support the work of the robot [4]. The autonomous system applied to the AUV can make it easier for users to operate, such as maneuvering the robot, avoiding other objects, taking pictures and videos and sending data to users wirelessly [5].

METHODOLOGY

Hardware Design

The following is the design of the entire hardware circuit on the underwater robot

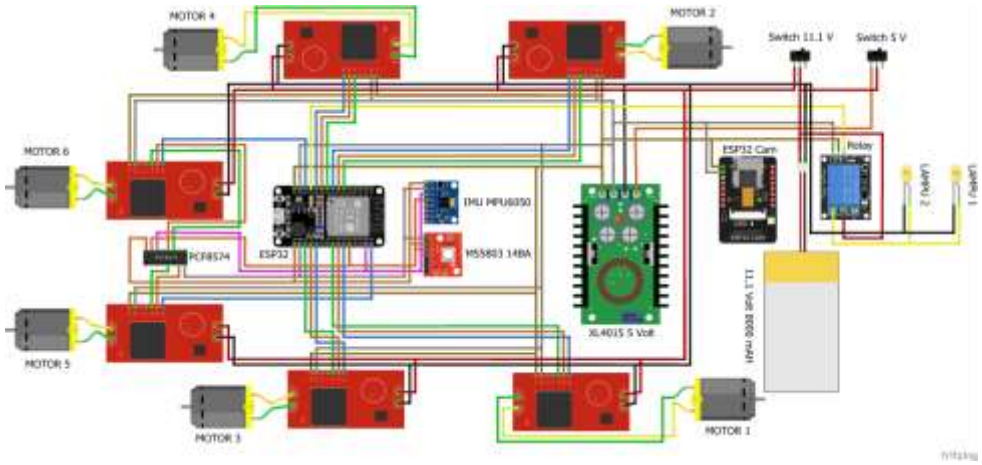

Figure. 1 The Overall Circuit of Underwater Robot Hardware

The explanation of the components contained in **Figure. 1**, including:

1. DOIT ESP32 DEVKIT is used as the main controller of the control system.

2. ESP32 Cam and OV2640 cam are used as image and video image data capture.
3. PCF8574 IO module is used as an additional GPIO pin.
4. MS5803 pressure sensor is used to measure the depth position of the robot.
5. IMPU MPU6050 sensor is used to measure the tilt of the robot and maintain the stability of the robot.
6. VNH2SP30 motor driver is used as a DC motor driver.
7. A 1100gph bilge pump DC motor is used to drive the robot.
8. Relay is used as a regulator of the condition of the lamp.
9. Lamp is used as a robot lighting.
10. Buck converter XL4015 is used to lower the voltage from 11.1 V to 5 V.
11. On-off switch is used to disconnect and connect electric current.
12. LiPo (Lithium Ion Polymer) battery is used as a voltage source for the robot.

Flowchart Design System

The following is a flow diagram of the underwater robot as shown in **Figure. 2**.

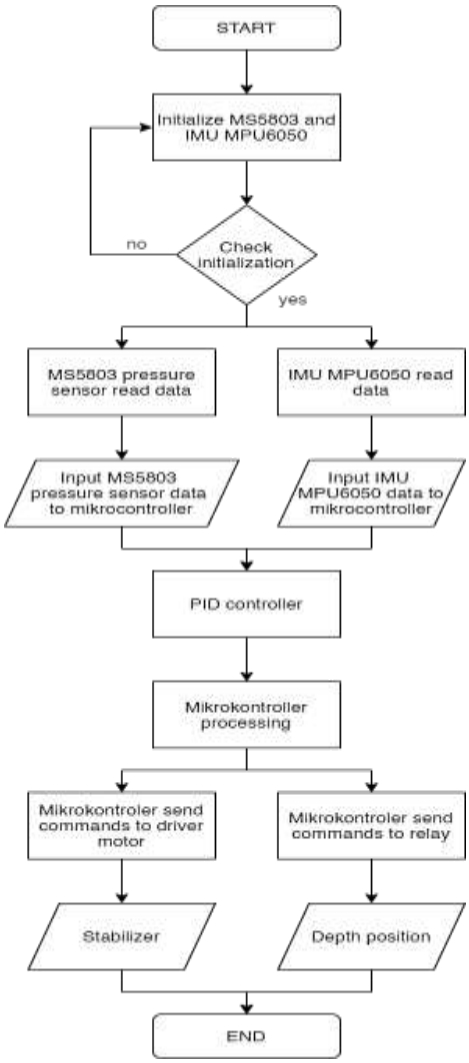

Figure. 2 Flowchart Design System Underwater Robot

Robot Motion Design

In designing the motion of the robot, six motors are used which are equipped with a propeller of 60 mm for each motor.

Table 1. Direction of Rotation of The Propeller to The Motor Thrust Force

Position Propeller	Motor Thrust Style	
	Clockwise	Anti-Clockwise
Motor 1	Down	Up
Motor 2	Up	Down
Motor 3	Up	Down
Motor 4	Down	Up
Motor 5	Forward	Backward
Motor 6	Backward	Forward

The formulation of the input function of each DC motor can be seen in **Table 2**.

Table 2. DC Motor Input Function

DC Motor	PID			Joystick
	Roll	Pitch	Depth	
1	+	+	+	
2	-	+	+	
3	+	-	+	
4	-	-	+	
5				+
6				+

RESULTS AND DISCUSSIONS

Underwater Robot Design Results

In designing the robot,1/2 inch PVC pipe and several pipe connections are used which are to form a robot frame. To protect the robot components that are not waterproof a watertight control box is used which has dimensions of 27 cm x 18.4 cm x 9.4 cm.

Figure. 3 Underwater Robot Design Result

PID Control Test Results

In the PID roll control test, it is done by providing different PID parameter values. Where this test was carried out five times. PID roll control testing is done by tilting the robot on a roll slope until it reaches a slope of about 30˚ then released and the resulting response system is seen. The data on the characteristic of the response system from each experiment in this test can be seen in **Table 3**.

Table 3. Characteristics of Roll PID Control Response System

No	PID Parameters	Rise Time	Peak Time	Settling Time	Overshoot
1	Kp 0.5, Ki 1, Kd 1	0.9702 s	1.34 s	6.7 s	17˚
2	Kp 0.001, Ki 0.01, Kd 0.5	1.0086 s	1.34 s	6.365 s	14˚
3	Kp 1, Ki 0.05, Kd 0.1	1.927 s	2.345 s	5.695 s	13˚
4	Kp 1, Ki 0.001, Kd 1	1.046 s	1.675 s	4.69 s	10˚
5	Kp 0.001, Ki 0.001, Kd 1	0.932 s	1.005 s	4.02 s	5˚

Based on **Table 3** above, it can be seen that in the PID roll test, the robot can maintain stability when given a PID parameter value of Kp 0.001, Ki 0.001 and Kd 1. Where the value of this parameter has obtained data on the characteristics of a good response system with a rise time value of 0.932 s, peak time of 1.005, settling time of 4.02 s and overshoot of 5˚.

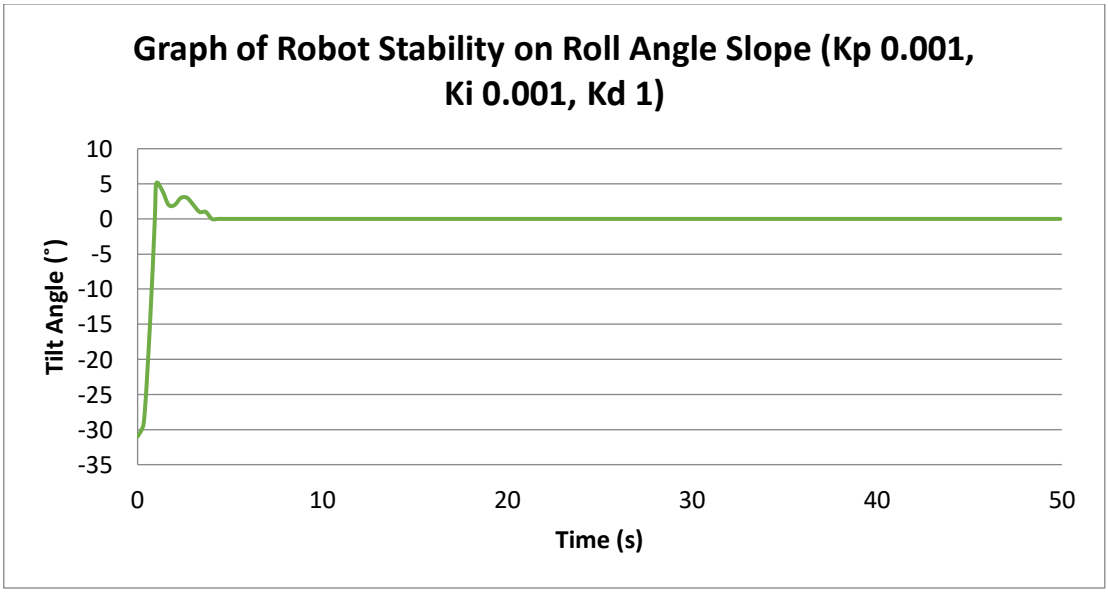

Figure. 4 Graph of Response System on Roll Slope

In the PID pitch control test, it is done by giving different PID parameter values. Where this test was carried out five times. PID pitch control testing is done by tilting the robot on a pitch slope until it reaches a slope of about 30˚ then released and the resulting response system is seen. The data on the characteristics of the response system for each PID pitch parameter are given as shown **Table 4**.

Table 4. Characteristics of Pitch PID Control Response System

No	PID Parameters	Rise Time	Peak Time	Settling Time	Overshoot
1	Kp 0.5, Ki 1, Kd 1	0.472 s	1.34 s	5.36 s	12˚
2	Kp 0.001, Ki 0.01, Kd 0.5	0.9703 s	1.34 s	5.695 s	16˚
3	Kp 1, Ki 0.05, Kd 0.1	0.5108 s	1.005 s	4.02 s	9˚
4	Kp 1, Ki 0.001, Kd 1	1.046 s	1.34 s	3.015 s	5˚
5	Kp 0.001, Ki 0.001, Kd 1	0.855 s	1.005 s	3.35 s	4˚

Based on **Table 4**, the robot can maintain stability very well when given a PID parameter value of Kp 0.001, Ki 0.001 and Kd 1. Where the value of this parameter has obtained data on the characteristics of a good response system with a fast rise time of 0.855 s, peak time of 1.005 s, settling time of 3.35 s and overshoot of 4˚. So that the PID value is applied to the system.

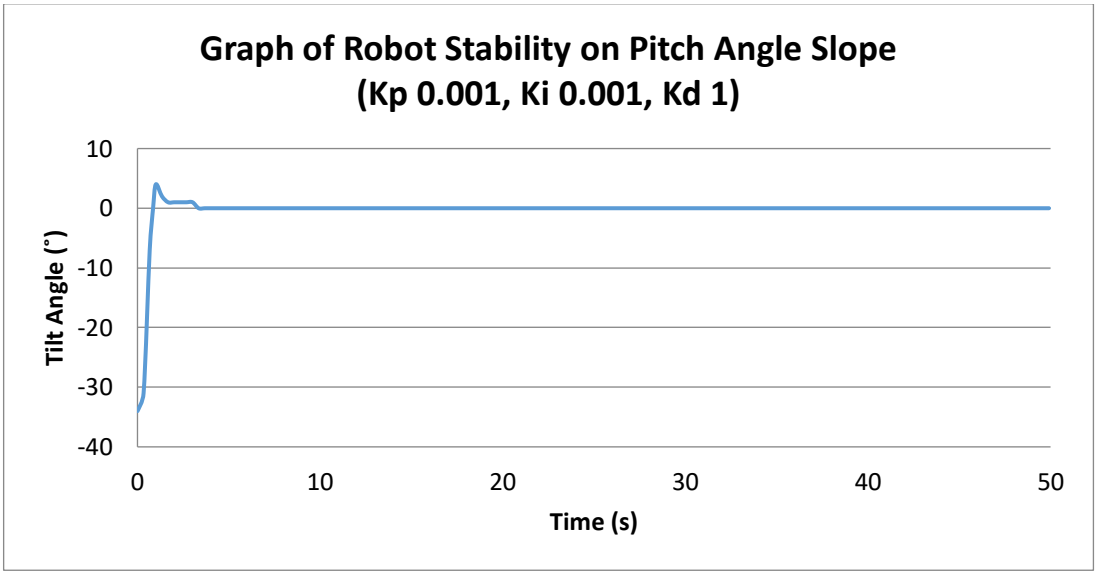

Figure. 5 Graph of Response System on Pitch Slope

In the PID control test, the depth position is carried out by providing different PID parameter values. Where this test was carried out five times. PID control testing for depth position is carried out when the robot is in a floating condition (0 cm depth) then gives a command in the form of a set point value for a depth of 5 cm by moving the slider widget on the blynk until it reaches number 5 and the resulting response system is seen. The data on the characteristics of the response system from each experiment in this test can be seen in **Table 5**.

Table 5. Characteristics of Depth Position PID Control Response System

No	PID Parameters	Rise Time	Peak Time	Settling Time	Overshoot
1	Kp 4, Ki 3, Kd 2	2.0938 s	7.705 s	49.8715 s	20% (1 cm)
2	Kp 3, Ki 2, Kd 2	2.0100 s	2.68 s	49.5365 s	20% (1 cm)
3	Kp 3, Ki 3, Kd 1	1.0888 s	2.68 s	49.5465 s	40% (2 cm)
4	Kp 5, Ki 1, Kd 3	0.2233 s	0.67 s	49.8815 s	40% (2 cm)
5	Kp 5, Ki 1, Kd 1	0.3769 s	0.67 s	49.2115 s	20% (1 cm)

PID control testing at the depth position is carried out by giving 5 cm depth position command using the slider widget on the blynk application on the smartphone. in the depth position PID test, the robot can maintain stability when given the PID parameter values Kp 5, Ki 1 and Kd 1. Where the value of this parameter has obtained good response system characteristic data worth a rise time of 0.3769 s, peak time of 0.67 s, settling time 49.2115 s and overshoot by 20% (1 cm).

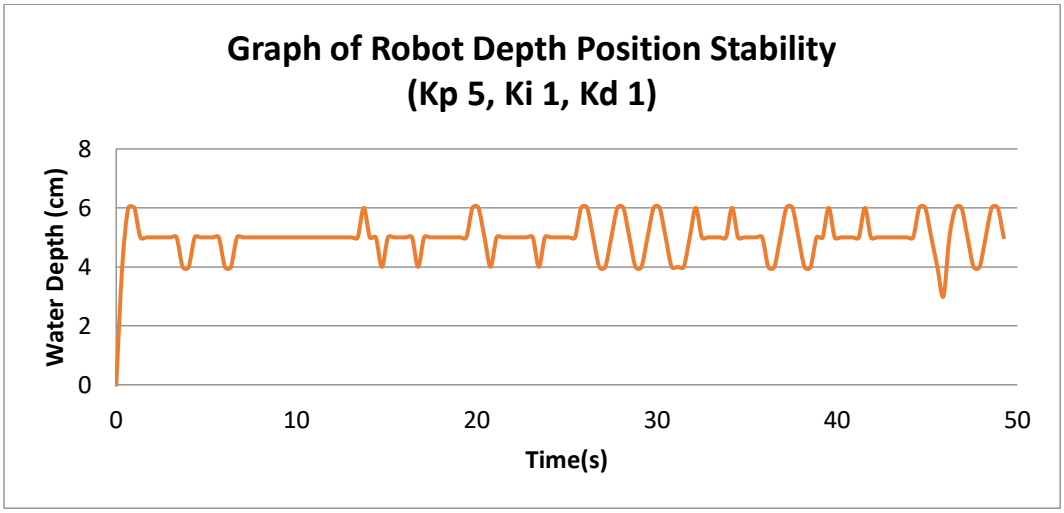

Figure. 6 Graph of Response System on Robot Depth Position

Stability Test Result Against Random Disturbance

Stability testing against random disturbances is carried out to determine the speed of the system response in maintaining the stability of the robot when there is a disturbance. Where the disturbance is given in the form of water waves generated by a DC motor. The value of the PID parameter used is the value that produces the best response in this control system, namely Kp_{roll} of 0.001, Ki_{roll} of 0.001, Kd_{roll} 1, Kp_{pitch} of 0.001, Ki_{pitch} of 0.001, Kd_{pitch} 1, Kp_{depth} of 5, Ki_{depth} of 1 and Kd_{depth} of 1.

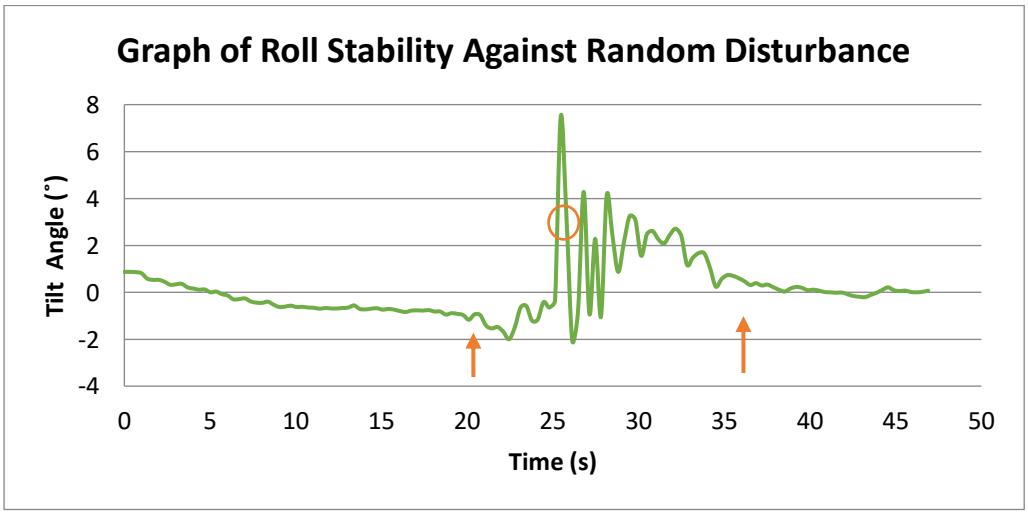

Figure. 7 Graph of Roll Stability Against Random Disturbance

In **Figure. 7**, it can be seen that in the second to 19.43 the robot is still in a stable condition and has not been disturbed. Then at the second to 19.765 the robot experienced instability due to the disturbance given until the second to 35.845 as indicated by the arrow, which resulted in a maximum slope error of 7.5˚. This error occurs because the disturbance given to the robot is greater than the robot's thrust, so the robot difficulty maintaining stability. Then the robot can be stable again at the second to 36.18.

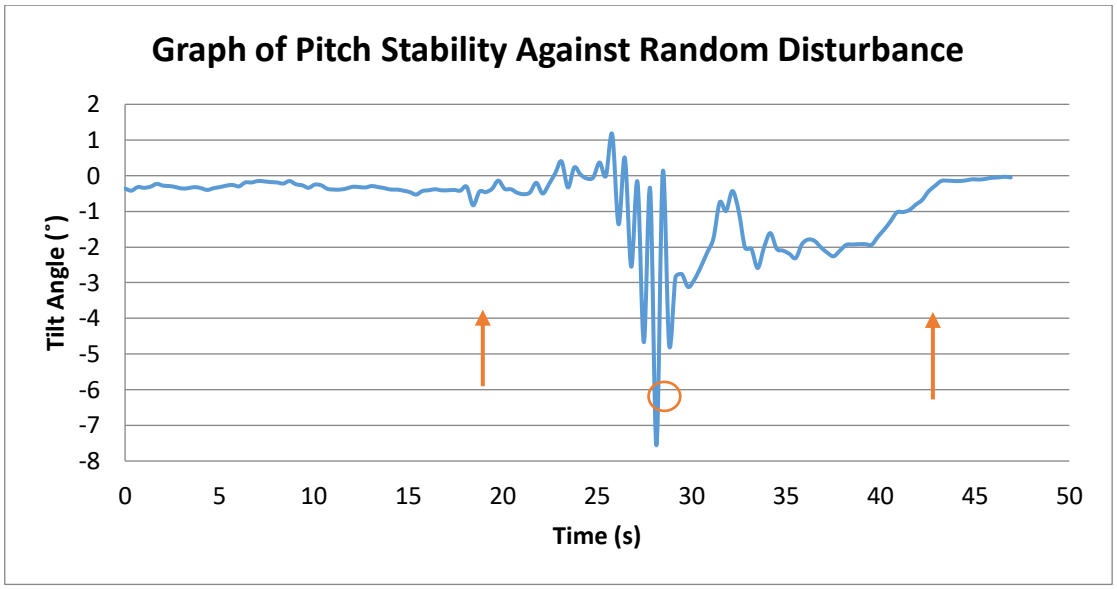

Figure. 8 Graph of Pitch Stability Against Random Disturbance

In the pitch stability graph as shown in **Figure. 8**, the robot is still stable and has not experienced disturbances until the second to 17.42. At the second 17.755 to 42.545 the robot experienced instability due to random disturbance given. Where in this condition the robot has a pitch slope error of 7.56˚. Then the robot can stabilize again at the second to 42.88.

CONCLUSION

The outcome of the number of layers study can be concluded that there are significant differences in the mechanical properties result. Tensile strength and bend ability of the welded metal show optimal when the layers increased. The results for tensile test shows that the highest point recorded is 460,831 MPa for 4 layers, while bend test without any defects recorded was 919.544 MPa for 4 layers, both using electrode ER70S-6. Based on the response optimizer done by this research, electrode ER70S-6 is the ideal electrode used in this study for tensile and bend.

REFERENCES

[1] ASM International, *Alloying: Understanding the Basics*. New York: ASM International,2001.
[2] DIN Standard, "Steels for General Structure Purposes: Quality Standard," in *Allgemeine Baustähle*, Dessau-Roßlau: Zementanlagenbau GmbH, 1980, pp. 2–15.
[3] A. Tjahjono, *Fisika Logam dan Alloy*. Jakarta: UIN Jakarta Press, 2013.
[4] E. Wen, R. Song, and W. Xiong, "Effect of Tempering Temperature on Microstructures and

Wear Behavior of a 500 HB Grade Wear-Resistant Steel," *Metals (Basel).*, vol. 9, no. 1, 2019, doi: 10.3390/met9010045.

[5] A. R. Chintha, "Metallurgical Aspects of Steels Designed to Resist Abrasion, and Impact-Abrasion Wear," *Mater. Sci. Technol. (United Kingdom)*, vol. 35, no. 10, pp. 1133–1148, 2019, doi: 10.1080/02670836.2019.1615669.

[6] A. Czupryński, "Microstructure and Abrasive Wear Resistance of Metal Matrix Composite Coatings Deposited on Steel Grade AISI 4715 by Powder Plasma Transferred Arc WeldingPart 2. Mechanical and Structural Properties of A Nickel-Based Alloy Surface Layer Reinforced with P," *Materials (Basel).*, vol. 14, no. 11, 2021, doi: 10.3390/ma14112805.

[7] Department of Defense Manufacturing Process Standard, *Millitary Specification*, MIL- STD-11. Washington DC: Department of Defense USA, 1979.

[8] B. Mvola, P. Kah, and J. Martikainen, "Dissimilar Ferrous Metal Welding Using Advanced Gas Metal Arc Welding Processes," *Rev. Adv. Mater. Sci.*, vol. 38, no. 2, pp. 125–137, 2014.

[9] M. T. Abdullah, M. L. N. Ajian, and P. E. Sarah, "Studies on The Effects of Multipass Welding on Mechanical Properties of Mild Steel on SMAW Joint," *J. Mech. Eng. Res. Dev.*, vol. 42, no. 5, pp. 202–204, 2019, doi: 10.26480/jmerd.05.2019.202.204.

[10] D. M. Devia, L. V Rodriguez-Restrepo, and E. Restrepo-Parra, "Methods Employed in Optical Emission Spectroscopy Analysis: a Review," *Ing. y Cienc.*, vol. 11, no. 21, pp. 239– 267, 2015.

[11] E. Bonnart, *Welding Principles and Practices*, 5th ed. New York: McGraw-Hill Education, 2018.

[12] J. F. Lancaster, *Metallurgy of Welding*, 3rd ed. London: George Allen & Unwin LTD, 1980.

[13] Kobelco, *Arc Welding of Specific Steels and Cast Irons*. Tokyo: KOBE Steel, Ltd., 2015.

[14] R. L. Brockenbrough and F. S. Merritt, *Structural Steel Designer's Handbook*, 3rd ed. New York: McGraw, Inc., 1999.

[15] J. S. Jensen, *Unitor Maritime Welding Handbook*, 14th ed. Lysaker: Wilhelmsen Ships Service, 2017.

[16] ASME Boiler and Pressure Vessel Code, *Qualification Standard for Welding and Brazing Procedures, Welders, Brazers, and Welding and Brazing Operators*. New York: The American Society of Mechanical Engineers, 2004.

[17] I. Gowrisankar, A. K. Bhaduri, V. Seetharaman, D. D. N. Verma, and D. R. G. Achar, "Effect of the Number of Passes on the Structure and Properties of Submerged Arc Welds ofAISI Type 316L Stainless Steel.," *Weld. J. (Miami, Fla)*, vol. 66, no. 5, 1987.

Available online at:
Al-Fiziya: Journal of Materials Science, Geophysics, Instrumentation and Theoretical Physics
Website: http://journal.uinjkt.ac.id/index.php/al-fiziya
Vol. 4 No. 2 Tahun 2021, 124 - 130

Assessment of Number of Layers on Tensile and Bend Strength of HB 500 and ST 42 Dissimilar Weldments

Cut Fitria [1,†], Arif Tjahjono [1], Iwan Setiawan [2]

[1]Department of Physics, Faculty of Science and Technology, Syarif Hidayatullah Islamic State University, Ir. H. Djuanda St, No.95, Cempaka Putih, Ciputat, South Tangerang, Banten 15412, Indonesia
[2]Laboratory of Calibration and Testing, Quality Assurance & K3LH, PT. Pindad (Persero), Gatot Subroto Street No.517, Bandung, West Java 40285, Indonesia
[†]cutfitria1@gmail.com

Submitted : September 2021; Revised : December 2021; Approved : December 2021; Available Online : December 2021

Abstrak. Penggabungan beberapa material dengan karakteristik berbeda sudah banyak dilakukan untuk kemajuan industri, terutama untuk mendapatkan karakteristik material yang lebih unggul dari sebelumnya. Salah satu teknik penggabungan yang paling umum adalah pengelasan. Penelitian ini untuk mengetahui kemampuan las pada baja yang berbeda dengan jumlah lapisan yang divariasikan antara 3 dan 4 lapis. Objek dari penelitian ini adalah sambungan las pelat baja tahan aus HB 500 dengan baja konstruksi ST 42 dimana ketebalan masing-masing material yaitu 10 mm. Pengelasannya dengan metode Gas Metal Arc Welding (GMAW) menggunakan logam pengisi ER 70 S di setiap lapisan dan kuat arus dari 90 A hingga 180 A di setiap sambungan. Pengujian tarik dan tekuk dilakukan sebagai karakterisasi daerah lasan untuk mengetahui sifat mekaniknya. Hasil pengujian memperlihatkan pengaruh yang signifikan dari jumlah lapisan terhadap kualitas sambungan. Nilai optimum terbentuk pada jumlah lapisan pengisi sebanyak 4 lapis dengan kakuatan tarik sebesar 448,37 - 473,292 MPa, tegangan luluh sebesar 305,767 - 317,493 MPa, perpanjangan 33,8 - 34,56%, dan mampu tekuk saat beban 874,498 - 919.544 MPa dengan sudut terbentuk yaitu 85,414° pada bagian dalam dan 86,14° pada bagian muka.
***Kata Kunci**: Baja HB 500, Baja ST 42, dan Pengelasan Logam Berbeda*

Abstract. The joining of several materials with different characteristics has been widely carried out for industrial progress, especially to obtain material characteristics that are superior to the previous one. One of the most common joining techniques is welding. This research was conducted to determine the weldability of different steels with the number of layers varying between 3 and 4 layers. The object of this research is the welded connection of HB 500 wear-resistant steel plate with ST 42 construction steel plate where the thickness of each material is 10 mm. Welding with the Gas Metal Arc Welding (GMAW) method employes ER 70 S filler metal in each layer and currents from 90 A to 180 A at each connection. Tensile and bending tests were carried out as a characterization of the weld area to determine its mechanical properties. The results show a significant effect of the number of layers on the quality of the connection. The optimum value is formed in the number of infill layers as much as 4 layers with tensile strength of 448.37 - 473.292 MPa, yield stress of 305.767 - 317.493 MPa, elongation of 33.8 - 34.56%, andable to bend under load 874,498 - 919,544 MPa with angle formed are 85.414° on the root and 86.14° on the face.
***Keywords**: HB 500 Steel,ST 42 Steel, and Dissimilar Weldments*

DOI : *10.15408/fiziya.v4i2. 22575*

P-ISSN: 2621-0215, E-ISSN: 2621-489X

INTRODUCTION

High strength low-alloy (HSLA) steel is one of alloy steel's development which designed to provide better mechanical properties required in the industry such as toughness, strength, formability, weldability and atmospheric corrosion resistance than conventional carbon steel [1]. Construction steel is one of HSLA steel which has good tensile strength and toughness with maximum carbon content is 0.2%. The application of this steel is based on consideration of its minimum tensile stress which is high enough, so that its toughness will be maximized. This steel is widely used in the construction of buildings, bridges, engine shafts and gears [2], [3].

Furthurmore, HSLA steel also has special characteristics such as wear resistance. Wear is one of the main demage forms that occurs in the mining, excavation and lifting industries whereas contributes to about 60% of total wear losses [4]. According to the mechanism of damage, wear is classified into corrosion, erosion, adhesion, abrasive, fretting, and fatigue. Another type of HSLA steel is wear-resistant steel. Advance researches and field tests indicate that the degree of wear, abrasion and abrasion-test of a material is linearly correlated with hardness [5]. Therefore, wear-resistant steel has a series name based on the level of hardness.

Dissimilar welds of wear-resistant steel and construction steel are widely employed in the mining of rock and the oil and gas wells in underground workings [6]. Nevertheless, the welding is quite complicated to do because the two materials have different mechanical properties that affect the weldability. The mechanical properties of the material shown in Table 1.

Table 1. Mechanical properties of HB 500 and ST 42 [2], [7]

Material	Hardness	Tensile Strength	Yield Stress	Elongation
	HB	Mpa	Mpa	%
HB 500	477 - 534	11.4090	9.0321	17
ST 42	123	415	290	20

The mechanical properties of dissimilar weld joints regard the critical factors of safety warranty and load ability. The investigation of the dissimilar weldment result by an arc welding method between HSLA and low-carbon steel revealed that the mechanical performance as though maximum load point, bend capability, and tensile strength are considerably improved by the process control (proper heat input and suitable electrode) rather than being dependent mainly on the material alloy element [8]. Besides, numerous studies also have attempted to explain the effect of number of welding layers influences on the performance of mechanical properties. Research has shown that the tensile strength of the joint increases along with the additional number of layers [9].

METHODS

Experimental Materials

The material for the purposes of this work, HB 500 wear resistant plate and ST 42 construction steel with a thickness of 10 mm were used. Both of materials were cut to

the obtain equivalent dimensions of 150 x 300 mm. Furthermore, an examination of the chemical composition was carried out using Optical Emission Spectroscopy by placing the lathe material at the mouth of the furnace which was fed with co-axial argon [10]. Optical Emission Spectroscopy reads the material elements by using wavelength and the percentage of content weight by using light intensity, the results given are listed in Table 2. Then, the weld bevel of square groove butt joint are made with a slope of 30° for all the involved materials.

Table 2. Chemical composition of the materials

Material	**Chemical Composition** wt%						
	Fe	C	Si	Mn	Cr	Ni	Mo
HB 500	97.46	0.147	0.309	0.328	0.982	0.183	0.281
ST 42	98.18	0.177	0.049	0.964	0.0082	0.0015	0.0012

In connection with the weldment using gas metal arc welding method, it requires a gas blanket to protect it from atmospheric contamination [11]. The type of gas used is CO2, accordance with the standards to be applied on carbon steel and low alloy steel materials in the form of sheet metal [12]. The welding wire used for this method is ER70S-6 with a diameter of 1 mm. Table 3 shows the typical chemical compositions and mechanical properties of the filler materials based on AWS A5,18:2005 and A5,20:2005 [13].

Table 3. Mechanical properties and chemical composition of ER70S-6 solid wire

Mechanical Properties			**Chemical Composition** wt%					
Tensile Strength	Yield Stress	Elongation						
ksi	ksi	%	C	Si	Mn	Cr	Ni	Mo
70	58	22	0.06 - 0.15	0.45 - 0.75	0.9 - 1.4	0.15	0.15	0.15

Welding Procedures

Groove butt joint is the type of weld joint used in this study. The use of sufficient transfer force creates a penetration where the weld material and base metal are fused throughout the entire depth of the joint. Consequently, the small transfer force creates a partial penetration where the edges are not formed optimally and the depth is less than the thickness of the joint [11], [14].

This research used gas metal arc welding technologies, two modes of welding were used, which generated different number of layers. The machine settings are first applied to the current strength from the lowest to the highest, then the welding process uses the down hand position. This method is equipped with a protective gas electrode coating to provide an easy-to-grab and stable arc [13]. This coating material also contains elements that can affect the transport of metal as it crosses the arc. Aswell as providing good mechanical and chemical properties to the alloy formed between the weld metal and the core of the rod at the electrode. When melted, the coating acts as a protection

against the atmosphere during welding by forming slag when it cools which further protects the weld during the cooling process [15].

(a) (b)

Figure 1. (a) Welding jigs for each plates, (b) test specimen of mechanical testing

Moreover, for welding quality corresponding to the standards, the welder employed a grinder to rarefaction the weld surface after the layer filled. The plates were fixed by the welding jigs (Figure 1a) and the weld edges were degreased and cleaned before doing the weldment. The weld gap for this method, is 1.5 mm. As for the use of shielding gas, the purity of CO2 gas is at least 99.8 vol% with flow rates and velocities of 20-25 l/min and 2 m/s, respectively. The distance between the tip of the contact and the base metal (wire extension) is 10-15 mm for the current used of 90 A to 180.

Mechanical Testing

The performance of the tensile and bend test were made by TRUMPF TruLaser 1030 according to the relevant standard ASME QW-463.l for Plates - Longitudinal Procedure Qualification [16]. In order to tensile test, the average values of yield strength, tensile strength, and elongation were obtained. Meanwhile, the bend test is used to obtain an overview of the ductility of the weld. Both tensile and bend test was performed on two samples from each welded joint, where one sample were loaded from the root side and one sample from the face side of the weld. The dimensions of the test specimen are shown in Figure 1b. Measurements were performed on anShimadzu Universal Testing Machine AGX.R testing device.

RESULTS AND DISCUSSIONS

Tensile Test

The average values of the tensile strength (TS), yield strength (YS), and elongation were computed by a static tensile test. According to the mentioned theory, the fracture of dissimilar weldment occurs in the base metal with lower mechanical properties value. The results of this research shown that ST 42 construction steel base metal is fractured, as well as both ER70S-6 and HB 500 wear resistant steel remained intact. Figure 2 shows the fracture specimens that localize the yield point to the sub-critical HAZ (SCHAZ).

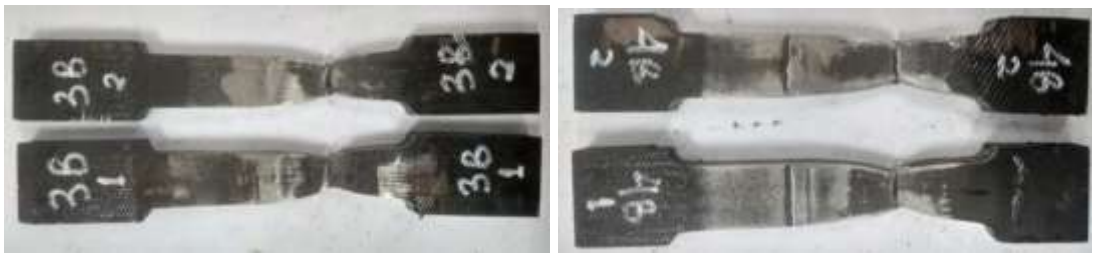

(a) (b)

Figure 2. (a) Fracture specimens for three layers weldment, (b) Fracture specimens for four layers weldment

On the one hand, the tensile test has qualified the standard because the results are exceeded the minimum ST 42 steel limit. On the other hand, the specimen with three layers weldment in quantity not as optimal as four layers weldment. Those values both in the root side and face side are shown in Table 4.

Table 4. Mechanical properties of the evaluated dissimilar welded joints of HB 500 and ST42 steel

Specimen	Tensile Strength	Average	YieldStress	Average	Elongation	Average
	Mpa		Mpa		%	
3 Layers	446.927	447.846	316.071	313.076	25.32	26.92
	448.766		310.081		28.52	
4 Layers	448.370	460.831	305.767	311.630	33.80	34.18
	473.292		317.493		34.56	

Maximum tensile strength was possessed by the specimen welded using four layer weldment. The number of layers of this experiment shows that the best tensile strength is reached by the increasing layer treatment.

Bend Test

The value of maximum force and angle formed were computed by guided bend, no die test. Because of the material used has a high hardness (for HB 500 steel), the fluctuation occurs on numerical data for the applied load to bend the specimen. This phenomenon caused the specimens had stroke on the weld metal ER70S-6 and base metal ST 42. The examination carried out on two sides of the part between the root and face of the specimen resulted in bending as shown in Figure 3.

(a) (b)

Figure 3. (a) Specimen with three layers weldment, (b) Specimen with four layers weldment

According to Figure 3, the specimen with three layers weldment in quality not as optimal as four layers weldment because the crack occurred in this specimen. Meanwhile, the four layers weldment had such an optimum results with no cracks occurring in either the weld metal, the heat affected area or the parent metal. The maximum force and angle formed when the deflection reaches its maximum point can be seen in Table 5.

Table 5. Maximum deflexion evaluation dissimilar weldedjoints of HB 500 and ST 42 steel

Specimen		**Maximum Force**	**Angle Formed**	**Defect**
		Mpa	Mpa	
3 Layers	Root	1003.41	79.08°	Crack
	Face	873.826	94.78°	Crack
4 Layers	Root	919.544	86.14°	No occur
	Face	874.496	85.41°	No occur

Regarding Table 5, the number of layers have an effect on the bending ability of a welding result. The sample with three layers present high risks of defect in service due to its HAZ. Nevertheless, the sample with four layers had good bending ability both in the root side and face side. Based on the previous research, as the number of layers increased, the tensile strength increased, while ductility and toughness decreases [17]. Hence, the examination diverge from the reviewed literature, this is possibly due to the number of layers in the experiment that leads to good performance of mechanical properties by using such an appropriate electrode for balancing both HB 500 and ST 42 steel.

CONCLUSION

The outcome of the number of layers study can be concluded that there are significant differences in the mechanical properties result. Tensile strength and bend ability of the welded metal show optimal when the layers increased. The results for tensile test shows that the highest point recorded is 460,831 MPa for 4 layers, while bend test without any defects recorded was 919.544 MPa for 4 layers, both using electrode ER70S-6. Based on the response optimizer done by this research, electrode ER70S-6 is the ideal electrode used in this study for tensile and bend.

REFERENCES

[1] ASM International, *Alloying: Understanding the Basics*. New York: ASM International,2001.
[2] DIN Standard, "Steels for General Structure Purposes: Quality Standard," in *Allgemeine Baustähle*, Dessau-Roßlau: Zementanlagenbau GmbH, 1980, pp. 2–15.
[3] A. Tjahjono, *Fisika Logam dan Alloy*. Jakarta: UIN Jakarta Press, 2013.
[4] E. Wen, R. Song, and W. Xiong, "Effect of Tempering Temperature on Microstructures and Wear Behavior of a 500 HB Grade Wear-Resistant Steel," *Metals (Basel).*, vol. 9, no. 1, 2019, doi: 10.3390/met9010045.
[5] A. R. Chintha, "Metallurgical Aspects of Steels Designed to Resist Abrasion, and Impact-Abrasion Wear," *Mater. Sci. Technol. (United Kingdom)*, vol. 35, no. 10, pp. 1133–1148, 2019, doi: 10.1080/02670836.2019.1615669.

[6] A. Czupryński, "Microstructure and Abrasive Wear Resistance of Metal Matrix Composite Coatings Deposited on Steel Grade AISI 4715 by Powder Plasma Transferred Arc WeldingPart 2. Mechanical and Structural Properties of A Nickel-Based Alloy Surface Layer Reinforced with P," *Materials (Basel).*, vol. 14, no. 11, 2021, doi: 10.3390/ma14112805.
[7] Department of Defense Manufacturing Process Standard, *Millitary Specification*, MIL- STD-11. Washington DC: Department of Defense USA, 1979.
[8] B. Mvola, P. Kah, and J. Martikainen, "Dissimilar Ferrous Metal Welding Using Advanced Gas Metal Arc Welding Processes," *Rev. Adv. Mater. Sci.*, vol. 38, no. 2, pp. 125–137, 2014.
[9] M. T. Abdullah, M. L. N. Ajian, and P. E. Sarah, "Studies on The Effects of Multipass Welding on Mechanical Properties of Mild Steel on SMAW Joint," *J. Mech. Eng. Res. Dev.*, vol. 42, no. 5, pp. 202–204, 2019, doi: 10.26480/jmerd.05.2019.202.204.
[10] D. M. Devia, L. V Rodriguez-Restrepo, and E. Restrepo-Parra, "Methods Employed in Optical Emission Spectroscopy Analysis: a Review," *Ing. y Cienc.*, vol. 11, no. 21, pp. 239– 267, 2015.
[11] E. Bonnart, *Welding Principles and Practices*, 5th ed. New York: McGraw-Hill Education, 2018.
[12] J. F. Lancaster, *Metallurgy of Welding*, 3rd ed. London: George Allen & Unwin LTD, 1980.
[13] Kobelco, *Arc Welding of Specific Steels and Cast Irons*. Tokyo: KOBE Steel, Ltd., 2015.
[14] R. L. Brockenbrough and F. S. Merritt, *Structural Steel Designer's Handbook*, 3rd ed. New York: McGraw, Inc., 1999.
[15] J. S. Jensen, *Unitor Maritime Welding Handbook*, 14th ed. Lysaker: Wilhelmsen Ships Service, 2017.
[16] ASME Boiler and Pressure Vessel Code, *Qualification Standard for Welding and Brazing Procedures, Welders, Brazers, and Welding and Brazing Operators*. New York: The American Society of Mechanical Engineers, 2004.
[17] I. Gowrisankar, A. K. Bhaduri, V. Seetharaman, D. D. N. Verma, and D. R. G. Achar, "Effect of the Number of Passes on the Structure and Properties of Submerged Arc Welds ofAISI Type 316L Stainless Steel.," *Weld. J. (Miami, Fla)*, vol. 66, no. 5, 1987.

Available online at:
Al-Fiziya: Journal of Materials Science, Geophysics, Instrumentation and Theoretical Physics
Website: http://journal.uinjkt.ac.id/index.php/al-fiziya
Vol. 4 No. 2 Tahun 2021, 131 - 139

The FLRW Universe Metric in 4+1 Spacetime Dimensional with Spherical Coordinate Invariance

Rangga Prasetya Alamsyah[1,†], Meini Aninda[1]
[1]Department of Physics, Faculty of Science and Technology, Syarif Hidayatullah State Islamic University Jakarta, Indonesia
[†]rangga.prasetya18@mhs.uinjkt.ac.id

Submitted : May 2021; Revised : September 2021; Approved : December 2021; Available Online : December 2021

Abstract. The Friedmann-Lemaître-Robertson-Walker (FLRW) universe metric is an abstraction of the distance between two points in a time-evolving universe. The evolution of the FLRW universe can be either expansion or contraction. In this article, the FLRW universe metric in 4+1 spacetime is formulated. When this metric is relatively one dimension higher than the original metric. The addition of these dimensions is based on the assumption that the laws of physics have the same shape in the higher dimensions. A mathematical modeling idea is based on a spatial 4-dimensional isotropic sphere system immersed in this 5-dimensional spatial system. Then, Minkowski's flat spacetime concept was used to couple the spatial dimensions with the temporal dimension. Thus, we find the FLRW universe metric in 4+1 spacetime. The result of formalism shows that there is a radius quantity in the extra metric dimension, and this radius quantity forms the angle with the other two spatial dimensions. Then, we also show that the dimension of the cosmic scale factor will always be relatively higher than the spatial dimension of the metric. This has implications for the expansion or contraction of the FLRW universe model which remains valid in high dimensions.

Keywords: *The FLRW Universe Metric, 4+1 Dimensional Spacetime, Expansion of The Universe, Contraction of The Universe, Higher Dimensional.*

Abstrak. Metrik alam semesta Friedmann-Lemaître-Robertson-Walker (FLRW) merupakan abstraksi jarak antara dua titik di alam semesta yang berevolusi terhadap waktu. Evolusi alam semesta FLRW dapat berupa ekspansi ataupun kontraksi. Pada artikel ini, diformulasikan metrik alam semesta FLRW dalam ruangwaktu 4+1 dimensi. Yang mana, metrik ini relatif lebih tinggi satu dimensi dari metrik aslinya. Penambahan dimensi tersebut berdasarkan pada asumsi bahwa hukum fisika memiliki bentuk yang sama dalam dimensi tinggi. Sebagai ide pemodelan matematis, yakni berdasarkan sistem bola isotropik 4 dimensi spasial yang terbenam pada sistem 5 dimensi spasial. Kemudian, digunakan konsep ruangwaktu datar Minkowski untuk mengkopel dimensi spasial dengan dimensi temporal. Sehingga, didapati metrik alam semesta FLRW dalam ruangwaktu 4+1 dimensi. Hasil formalisme menunjukan bahwa adanya kuantitas radius dalam dimensi ekstra metrik, dan kuantitas radius ini membentuk sudut dengan dua dimensi spasial lainnya. Selain itu, kami juga menunjukan bahwa dimensi faktor skala kosmis akan selalu relatif lebih tinggi dari dimensi spasial metrik. Hal ini berimplikasi pada ekspansi ataupun kontraksi dari model alam semestra FLRW yang tetap berlaku dalam dimensi tinggi.
Kata Kunci: *Metrik Alam Semesta FLRW, Ruangwaktu 4+1 Dimensi, Ekspansi Alam Semesta, Kontraksi Alam Semesta, Dimensi Tinggi.*

DOI : *10.15408/fiziya.v4i2.20554*

P-ISSN: 2621-0215, E-ISSN: 2621-489X

INTRODUCTION

The FLRW universe metric is a model of the distance between two points in the universe that are evolving with time. The evolution of the FLRW universe can be either expansion or contraction [1]. This metric concept was first formulated by Friedmann, Lemaître, Robertson, and Walker. Therefore, this metric is referred to as the FLRW universe metric. However, this metric idea was first coined in 1930 by Robertson and Walker. The FLRW universe metric has the main assumptions on which it is based, namely the principles of homogeneity and isotropic space [2][3]. In other words, there is an even distribution of matter throughout the universe, and the distance from the center of the universe to the distribution of matter in all directions will always be the same on a large scale. Based on the results of astronomical physical observations, the FLRW universe metric is a metric model that is most suitable to the real conditions of the universe [4]. The FLRW universe metric is formulated in 3+1 dimensional spacetime [5]. Where the evolution of the universe can be observed.

Related to the topic discussed in this article, technically formulate the metric of the FLRW universe in high dimensions. From the metric of the FLRW universe which is formulated in the spacetime dimension of 3+1, to the metric in the dimension of spacetime of 4+1. The addition of this dimension is based on the assumption that the laws of physics apply equally to the higher dimensions [6]. Which the essential goal is to ensure the evolution of the FLRW universe that takes place in high dimensions. The idea of the metric formulation of the FLRW universe in 4+1 dimensional spacetime in this article is to use the modeling of a spatial 4-dimensional isotropic sphere system that is immersed in a 5-dimensional spatial system. Then, Minkowski's flat spacetime concept was used to couple the spatial dimensions with the temporal dimensions.

This high-dimensional concept was inspired by what Kaluza did in 1921. Where Kaluza hypothesized that the universe is not only 3+1 dimensions of spacetime. Based on this hypothesis, Kaluza conducted a unification experiment between a gravitational entity and an electromagnetic entity in a 4+1 dimensional spacetime [7]. In 1926, Klein collaborated with Kaluza and contributed to the idea that the existence of higher dimensions exists on a microscopic scale. The dimensions of the extra space are hypothesized to be circular in a circle with a radius of a very small value [6]. This Kaluza-Klein idea became the hypothesis for the existence of a high-dimensional universe N+1 that world physicists now agree on. The purpose of this study is to prove that the expansion or contraction of the FLRW model of the universe is valid in high dimensions.

FORMALISM

Spatial 4 Dimension System Immersed in 5 Spatial Dimension System

Fundamental mathematical modeling of the metric of the FLRW universe, which is a 4-dimensional isotropic sphere system immersed in a 5-dimensional spatial system. To achieve this, depart from a vector function in Euclid's 5 spatial plane dimensions [8]:

$$x_i = x_1 + x_2 + x_3 + x_4 + x_5 \tag{1}$$

Then to get the metric vector function from Eq. (1), namely by using the differential method to Eq. (1). The differential form describing the metric vector function of Eq. (1) is written:

$$dx_i = dx_1 + dx_2 + dx_3 + dx_4 + dx_5 \tag{2}$$

Since the metric tensor function is the outer product of two metric vectors, the formula for the metric tensor function is expressed in [9]:

$$\begin{aligned} dx \otimes dx &= \eta^{\mu\nu} dx_\mu dx_\nu \\ (dx)^2 &= \eta^{\mu\nu} dx_\mu dx_\nu \end{aligned} \tag{3}$$

Where, the metric contravariance tensor $\eta^{\mu\nu}$ in the matrix representation is in the form of:

$$\eta^{\mu\nu} = \begin{pmatrix} \eta^{11} & \cdots & \eta^{1n} \\ \vdots & \ddots & \vdots \\ \eta^{m1} & \cdots & \eta^{mn} \end{pmatrix} \tag{4}$$

Based on Eq. (3), the metric tensor form of Eq. (2) can be formulated:

$$(dx_i)^2 = (dx_1)^2 + (dx_2)^2 + (dx_3)^2 + (dx_4)^2 + (dx_5)^2 \tag{5}$$

Then, the radius quantity of an isotropic sphere in 5 spatial dimensions can be represented as:

$$R^2 = x_1^2 + x_2^2 + x_3^2 + x_4^2 + x_5^2 \tag{6}$$

By using the differential method of Eq. (6), a mathematical form is found:

$$0 = xdx_1 + xdx_2 + xdx_3 + xdx_4 + xdx_5 \tag{7}$$

Eq. (7) can be rewritten as:

$$dx_5 = -\frac{x_1 dx_1 + x_2 dx_2 + x_3 dx_3 + x_4 dx_4}{x_5} \tag{8}$$

Then, the results of the integral evaluation of Eq. (8) namely:

$$x_5 = -\frac{\left(x_1\right)^2 + \left(x_2\right)^2 + \left(x_3\right)^2 + \left(x_4\right)^2}{2x_5} \tag{9}$$

By substituting Eq. (9) into Eq. (5), we find the metric tensor of the FLRW universe in Cartesian coordinates:

$$\left(dx_i\right)^2 = \left(dx_1\right)^2 + \left(dx_2\right)^2 + \left(dx_3\right)^2 + \left(dx_4\right)^2 + \frac{1}{\left(2x_5\right)^2}\left[\sum_{j=1}^{4} d\left(x_j\right)^2\right]^2 \tag{10}$$

Spherical Coordinate Transformation Invariance

To get the transformation result from Eq. (10) in the form of a metric tensor in spherical coordinates, that is, it departs from the formulation of the fundamental transformation:

$$\begin{aligned} x_1 &= r\sin\theta\cos\phi\cos\alpha \\ x_2 &= r\sin\theta\sin\phi\cos\alpha \\ x_3 &= r\cos\theta\cos\alpha \end{aligned} \tag{11}$$

And:

$$r^2 = \left(x_1\right)^2 + \left(x_2\right)^2 + \left(x_3\right)^2 + \left(x_4\right)^2 \tag{12}$$

Then, for the formulation of transformation x_4 to spherical coordinates, starting from a 4-dimensional spatial vector function in Cartesian coordinates [10]:

$$\left(x_i\right)^2 = \left(x_1\right)^2 + \left(x_2\right)^2 + \left(x_3\right)^2 + \left(x_4\right)^2 \tag{13}$$

By substituting Eq. (11) into Eq. (13), it is obtained:

$$\left(x_i\right)^2 = \left(r\sin\theta\cos\phi\cos\alpha\right)^2 + \left(r\sin\theta\sin\phi\cos\alpha\right)^2 + \left(r\cos\theta\cos\alpha\right)^2 + \left(x_4\right)^2 \tag{14}$$

Based on Eq. (12) and Eq. (14) which is simplified by using the trigonometric theorem, a mathematical formulation is found:

$$\begin{aligned} r^2 &= r^2\cos^2\alpha[\sin^2\theta(\cos^2\phi+\sin^2\theta)+\cos^2\theta]+\left(x_4\right)^2 \\ r^2 &= r^2\cos^2\alpha(\sin^2\theta+\cos^2\theta)+\left(x_4\right)^2 \\ r^2 &= r^2\cos^2\alpha+\left(x_4\right)^2 \end{aligned} \tag{15}$$

After the two sides are reduced by the term $r^2\cos^2\theta$, we find the transformation form for the extra dimension x_4 to the following spherical coordinates:

$$\begin{aligned} \left(x_4\right)^2 &= r^2(1-\cos^2\alpha) \\ \left(x_4\right)^2 &= r^2\sin^2\alpha \\ x_4 &= r\sin\alpha \end{aligned} \tag{16}$$

Then, by differentiating Eq. (11) and Eq. (16), we find the following line elements:

$$\begin{aligned} dx_1 &= \sin\theta\cos\phi\cos\alpha\ dr + r\cos\theta\cos\phi\cos\alpha\ d\theta \\ &\quad + (-r\sin\theta\sin\phi\cos\alpha)\ d\phi + (-r\sin\theta\cos\phi\sin\alpha)\ d\alpha \end{aligned} \tag{17}$$

$$\begin{aligned} dx_2 &= \sin\theta\sin\phi\cos\alpha\ dr + r\cos\theta\sin\phi\cos\alpha\ d\theta \\ &\quad + r\sin\theta\cos\phi\cos\alpha\ d\phi + (-r\sin\theta\sin\phi\sin\alpha)\ d\alpha \end{aligned} \tag{18}$$

$$\begin{aligned} dx_3 &= \cos\theta\cos\alpha\ dr + (-r\sin\theta\cos\alpha)\ d\theta \\ &\quad + (-r\cos\theta\sin\alpha)\ d\alpha \end{aligned} \tag{19}$$

$$dx_4 = \sin\alpha\ dr + r\cos\alpha\ d\alpha \tag{20}$$

Based on the mathematical axiom of Eq. (3), the metric tensor function in spherical coordinates is given by the following set of formulations:

$$\begin{aligned} \left(dx_1\right)^2 &= \sin^2\theta\cos^2\phi\cos^2\alpha\ dr^2 + r^2\cos^2\theta\cos^2\phi\cos^2\alpha\ d\theta^2 \\ &\quad + r^2\sin^2\theta\sin^2\phi\cos^2\alpha\ d\phi^2 + r^2\sin^2\theta\cos^2\phi\sin^2\alpha\ d\alpha^2 \\ &\quad - 2r\sin^2\theta\cos^2\phi\sin\alpha\cos\alpha\ dr d\alpha - 2r^2\sin\theta\cos\theta\cos^2\phi\sin\alpha\cos\alpha\ d\theta d\alpha \\ &\quad - 2r\sin^2\theta\sin\phi\cos\phi\cos^2\alpha\ dr d\phi - 2r^2\sin\theta\cos\theta\sin\phi\cos\phi\cos^2\alpha\ d\theta d\phi \\ &\quad + 2r\sin\theta\cos\theta\sin\phi\cos\phi\cos^2\alpha\ dr d\theta \end{aligned} \tag{21}$$

$$\begin{aligned}(dx_2)^2 &= \sin^2\theta\sin^2\phi\cos^2\alpha\ dr^2 + r^2\cos^2\theta\sin^2\phi\cos^2\alpha\ d\theta^2 \\ &+ r^2\sin^2\theta\cos^2\phi\cos^2\alpha\ d\phi^2 + r^2\sin^2\theta\sin^2\phi\sin^2\alpha\ d\alpha^2 \\ &- 2r\sin^2\theta\sin^2\phi\sin\alpha\cos\alpha\ dr d\alpha - 2r^2\sin\theta\cos\theta\sin^2\phi\sin\alpha\cos\alpha\ d\theta d\alpha \\ &+ 2r\sin^2\theta\sin\phi\cos\phi\cos^2\alpha\ dr d\phi + 2r^2\sin\theta\cos\theta\sin\phi\cos\phi\cos^2\alpha\ d\theta d\phi \\ &+ 2r\sin\theta\cos\theta\sin^2\phi\cos^2\alpha\ dr d\theta - 2r^2\sin^2\theta\cos\theta\sin\phi\cos\phi\sin\alpha\cos\alpha\ d\phi d\alpha\end{aligned} \tag{22}$$

$$\begin{aligned}(dx_3)^2 &= \cos^2\theta\cos^2\alpha\ dr^2 + r^2\sin^2\theta\cos^2\alpha\ d\theta^2 + r^2\cos^2\theta\sin^2\alpha\ d\alpha^2 \\ &- 2r\sin\theta\cos\theta\cos^2\alpha\ dr d\theta - 2r\cos^2\theta\sin\alpha\cos\alpha\ dr d\alpha \\ &+ 2r^2\sin\theta\cos\theta\sin\alpha\cos\alpha\ d\theta d\alpha\end{aligned} \tag{23}$$

$$(dx_4)^2 = \sin^2\alpha\ dr^2 + r^2\cos^2\alpha\ d\alpha^2 + 2r\sin\theta\cos\alpha\ dr d\alpha \tag{24}$$

Then, by substituting Eq. (11), (16), (21-24) into Eq. (10), we get the formalism of the metric tensor in the following simplification results:

$$(dx_i)^2 = R^2(t)\left(\frac{1}{1-Mr^2}\ dr^2 + r^2\cos^2\alpha\sin^2\theta\ d\phi^2 + r^2\cos^2\alpha\ d\theta^2 + r^2\ d\alpha^2\right) \tag{25}$$

Where:

$$R(t) = r^2 + (x_5)^2 \tag{26}$$

And the curvature constant M which represents the shape of the space:

$$M = \begin{cases} 1 \leftrightarrow \text{Positive Curvature Space} \\ 0 \leftrightarrow \text{Flat Space} \\ -1 \leftrightarrow \text{Negative Curvature Space} \end{cases} \tag{27}$$

The relation between Eq. (25) and Eq. (27) is obtained from positive R^2 in Eq. (6) which can be converted into negative R^2. If M = 0 is determined, then a 4-dimensional isotropic spherical system is found immersed in a 5-dimensional Euclid system. Then to couple the temporal dimension with the spatial dimension, which is based on Minkowski's flat spacetime metric in the 4+1 dimension [9]:

$$(ds)^2 = -(c\ dt)^2 + (dx_i)^2 \tag{28}$$

By substituting Eq. (25) into Eq. (28), we find the metric of the universe FLRW in the spacetime dimension 4+1 at the spherical coordinates:

$$(ds)^2 = -(c\,dt)^2 + R^2(t)\left[\frac{1}{1+Mr^2}\,dr^2 + r^2\left(\cos^2\alpha\sin^2\theta\,d\phi^2 + \cos^2\alpha\,d\theta^2 + d\alpha^2\right)\right] \tag{29}$$

RESULT

This formalism yields the parameters $R(t)$ and M, which are the cosmic scale factor and the spatial curvature constant. For this context, the cosmic scale factor $R(t)$ is the sum of the radius r^2 of the spatial 4-dimensional system with the radius quantity in the spatial dimension $(x_5)^2$, and the cosmic scale factor $R(t)$ is a time-evolving quantity. The first significant difference between the metrics of the FLRW universe in dimensions 3+1 and 4+1 lies in the scale factor $R(t)$. The scale factor $R(t)$ in dimension 3+1 satisfies $r^2 + (x_4)^2$, with the definition of radius r^2 as $(x_1)^2 + (x_2)^2 + (x_3)^2$ [8]. Meanwhile, the scale factor $R(t)$ in the 4+1 spacetime dimension fulfills Eq. (26). Therefore, the scale factor $R(t)$ can be interpreted as a radius quantity with a dimension that is relatively higher than the FLRW metric spatial dimension, to parameterize the radial evolution of the universe. In other words, metric expansion or contraction remains valid in the 4+1 dimension. Based on the pattern of comparisons between the 3+1 and 4+1 dimensional metrics, it might be intuitive to expect that in the other higher dimensions the evolution of the metric will hold over time. The second significant difference lies in the $R^2r^2d\alpha^2$ term in Eq. (29), where the $R^2r^2d\alpha^2$ term only exists in the 4+1 spacetime dimension. It means that there is a radius quantity in the extra dimension $d\alpha^2$ which is orthogonal to the other dimensions. The final significant difference between the metric of the FLRW universe in the dimensions 3+1 and 4+1 is at the angle $\cos^2\alpha$ formed by the extra dimension $d\alpha^2$ with dimension $d\phi^2$ and dimension $d\theta^2$. Where this does not exist in the 3+1 dimension. Based on the results of formalism, the addition of this dimension does not have an impact on the curvature constant of space M. In other words, the curvature constant of space M applies generally to each dimension.

CONCLUSION

Based on the results obtained from this research, it can be concluded that the addition of dimensions in the metric formalism of the FLRW universe has an impact on the radius r^2 in the scale factor $R(t)$ which experiences an increase in the radius $(x_5)^2$ quantity. Thus, it has implications for the dimension of the cosmic scale factor which will always be relatively higher than the spatial dimension of the metric tensor. In other words, the expansion or contraction of the FLRW universe model remains valid in high

dimensions. Also, the metric tensor of the FLRW universe has the addition of the extra-dimensional term $R^2r^2d\alpha^2$ and the angle $\cos^2\alpha$ which are formed by the extra dimension $d\alpha^2$ with dimensions $d\phi^2$ and dimensions $d\theta^2$. As an application of this 4+1 dimensional FLRW universe metric, it can be used as an asymptotic spacetime for the 4+1 dimensional Schwarzschild spacetime and the 4+1 dimensional Reissner-Nordström spacetime**.**

ACKNOWLEDGMENTS

Appreciation and thanks the author gave to Prof. Dr. Husin Alatas as an Advisor regarding the general theory of relativity. As well as thank you to Haifa Rahma which has contributed as a language corrector to this article.

REFERENCES

[1] H. Alatas, A. K. Falah, T. Wibowo, M. A. Qohhar, and B. E. Gunara, "Coordinate-time lapse function of FLRW accelerated expanding universe in dRGT massive gravity theory," *Int. J. Mod. Phys. D*, vol. 29, no. 10, 2020, doi: 10.1142/S021827182050073X.

[2] B. L'Huillier and A. Shafieloo, "Model-independent test of the FLRW metric, the flatness of the Universe, and non-local estimation of H0rd," *J. Cosmol. Astropart. Phys.*, vol. 2017, no. 1, 2017, doi: 10.1088/1475-7516/2017/01/015.

[3] Q. Wang, "Reformulation of the Cosmological Constant Problem," *Phys. Rev. Lett.*, vol. 125, no. 5, 2020, doi: 10.1103/PhysRevLett.125.051301.

[4] S. Cao *et al.*, "Direct test of the FLRW metric from strongly lensed gravitational wave observations," *Sci. Rep.*, vol. 9, no. 1, 2019, doi: 10.1038/s41598-019-47616-4.

[5] H. het Lam and T. Prokopec, "Singularities in FLRW spacetimes," *Phys. Lett. Sect. B Nucl. Elem. Part. High-Energy Phys.*, vol. 775, 2017, doi: 10.1016/j.physletb.2017.10.070.

[6] S. Weinberg, "Massless particles in higher dimensions," *Phys. Rev. D*, vol. 102, no. 9, 2020, doi: 10.1103/PhysRevD.102.095022.

[7] J. Zhu *et al.*, "X-ray reflection spectroscopy with Kaluza–Klein black holes," *Eur. Phys. J. C*, vol. 80, no. 7, 2020, doi: 10.1140/epjc/s10052-020-8198-x.

[8] R. Anugraha, *Pengantar Teori Relativitas dan Kosmologi*. Gadjah Mada University Press, 2005.

[9] I. L. Zulfa, R. P. Alamsyah, and A. Fitriani, "Solusi Metrik Kerr-Newman Untuk Dimensi Ruang-waktu 3+1 Dengan Invariansi Rotasi Anisotropik," *Al-Fiziya J.*

Mater. Sci. Geophys. Instrum. Theor. Phys., vol. 3, no. 2, 2020, doi: 10.15408/fiziya.v3i2.18600.

[10] I. L. Saptiani, "Solusi geometri schwarzschild untuk dimensi 4+1 dengan invarian rotasi isotropik," 2019.


9 772621 489007


9 772621 021009